

Forged by Feedback: Stellar Properties of Brightest Group Galaxies in Cosmological Simulations

RUXIN BARRÉ ,¹ ARIF BABUL ,^{1,*} GHASSEM GOZALIASL ,^{2,3} ALEXIS FINOGUENOV ,³ ROMEEL DAVÉ ,^{4,5} AVIV PADAWER-BLATT ,¹ DOUGLAS RENNEHAN ,⁶ VIDA SAEEDZADEH ,⁷ RENIER T. HOUGH ,^{8,9} AND THOMAS R. QUINN ,¹⁰

¹ *Astronomy Research Centre, Department of Physics and Astronomy, University of Victoria, 3800 Finnerty Road, Victoria, BC, V8P 1A1, Canada*

² *Department of Computer Science, Aalto University, PO Box 15400, Espoo, FI-00 076, Finland*

³ *Department of Physics, University of Helsinki, Royal Observatory, Blackford Hill, Edinburgh, EH9 3HJ, United Kingdom*

⁴ *Institute of Astronomy, University of Edinburgh, Royal Observatory, Blackford Hill, Edinburgh, EH9 3HJ, United Kingdom*

⁵ *Department of Physics and Astronomy, University of the Western Cape, Bellville 7535, South Africa*

⁶ *Center for Computational Astrophysics, Flatiron Institute, 162 Fifth Avenue, New York, NY, 10010, USA*

⁷ *Department of Physics and Astronomy, Johns Hopkins University, 3400 N. Charles Street, Baltimore, MD, 21218, USA*

⁸ *Centre for Space Research, North-West University, Potchefstroom, 2520, South Africa*

⁹ *National Institute for Theoretical and Computational Sciences (NITheCS), Potchefstroom, 2520, South Africa*

¹⁰ *Astronomy Department, University of Washington, Box 351580, Seattle, WA, 98195-1580*

ABSTRACT

We investigate how different galaxy formation models impact the stellar properties of brightest group galaxies (BGGs) in four cosmological simulations: ROMULUS, SIMBA, SIMBA-C, and OBSIDIAN. The stellar masses, specific star formation rates, and mass-weighted stellar ages of the simulated BGGs are analysed alongside those of observed BGGs from X-ray-selected galaxy groups in the COSMOS field. We find that the global properties and underlying evolutionary pathways of simulated BGG populations are strongly impacted by the strength and mechanism of their respective active galactic nucleus (AGN) feedback models, which play a critical role in regulating the growth of massive galaxies. OBSIDIAN's sophisticated three-regime AGN feedback model achieves the highest overall agreement with COSMOS observations, matching stellar property distributions, quenched fractions, and the evolution of star formation in increasingly massive systems. We find evidence suggesting that BGG populations of OBSIDIAN and COSMOS undergo a gradual decline in star formation with stellar mass, in contrast to SIMBA and SIMBA-C, which display rapid quenching linked to the onset of powerful AGN jet feedback. By comparison, ROMULUS produces highly star-forming, under-quenched BGGs due to the inefficiency of its thermal AGN feedback in preventing cooling flows from fuelling BGG growth. The success of the OBSIDIAN simulation demonstrates the importance of physically motivated subgrid prescriptions for realistically capturing the processes that shape BGGs and their dynamic group environments.

Keywords: Galaxies (573) — Galaxy evolution (594) — Galaxy groups (597) — Brightest cluster galaxies (181) — Hydrodynamical simulations (767) — Galaxy quenching (2040)

1. INTRODUCTION

The development of realistic galaxy formation models has seen significant progress over the last two decades. Modern cosmological hydrodynamic simulations have

enabled us to strengthen our understanding of the complex interplay of physical processes that govern the formation and evolution of galaxies. Simulations comprise four types of gravitationally interacting particles that describe collisionless dark matter, stars, and supermassive black holes (SMBHs), and collisional, hydrodynamically interacting gas. Galaxies form by numerically solving the coupled hydrodynamic and gravity equations that govern the evolution of these components. Additionally, some components are subjected to analytical subgrid physics prescriptions, which model sub-resolution processes on the simulations' resolved scales,

Corresponding author: Ruxin Barré
 Email: barreruxin11@uvic.ca

* Leverhulme Visiting Prof., Institute for Astronomy, University of Edinburgh, Royal Observatory, Blackford Hill, Edinburgh, EH9 3HJ, United Kingdom

Infosys Visiting Chair Professor, Department of Physics, Indian Institute of Science, Bangalore, 560012, India

such as heating and cooling, stellar and active galactic nucleus (AGN) feedback, and star formation (R. S. Somerville & R. Davé 2015; M. Vogelsberger et al. 2020; B. D. Oppenheimer et al. 2021; S. L. Jung et al. 2022; R. A. Crain & F. van de Voort 2023).

Most large-scale simulations (e.g. I. G. McCarthy et al. 2017; M. Tremmel et al. 2017; A. Pillepich et al. 2018a; R. Davé et al. 2019; R. T. Hough et al. 2023; R. Kugel et al. 2023; D. Rennehan et al. 2024) aim to reproduce the entire spectrum of galaxy types and environments observed in our universe. To fix the various parameters in the subgrid models, the simulations are typically calibrated to reproduce two or three important observable relationships and characteristics of galaxies (R. A. Crain & F. van de Voort 2023; R. Kugel et al. 2023). This calibration approach is beneficial in simulating a broadly realistic galaxy population over cosmic time; however, to further improve our galaxy formation models, it is crucial to examine how subsets of the wider galaxy population and their distinct environments are represented and treated.

One such subset consists of some of the brightest and most massive galaxies in today's universe, found deep in the potential wells central to gravitationally bound groups of galaxies. Up to half of all galaxies in the low redshift universe reside in groups, with many more transitioning through groups (M. Bianconi et al. 2018). Correctly modelling these brightest group galaxies (BGGs), which play significant roles in shaping their group environments, is thus essential for completing our understanding of galaxy evolution. Despite this, only recently has focus been placed on understanding the evolution of BGGs and investigating their depiction in galaxy formation models (e.g. H. E. Loparelo et al. 2015; G. Gozaliasl et al. 2016, 2018, 2024, 2025; C. Nipoti 2017; S. L. Jung et al. 2022; S. I. Loubser et al. 2022; V. Olivares et al. 2022; M. Einasto et al. 2024) independently from that of the extensively studied central galaxies residing in galaxy-scale haloes or larger and more massive cluster environments (see C. Bildfell et al. 2008; C. Ragone-Figueroa et al. 2013, 2018, 2020; A. Gallazzi et al. 2014; D. Martizzi et al. 2014; L. O. V. Edwards et al. 2020; D. Rennehan et al. 2020; I. Marini et al. 2021).

It has been well established by observational and simulation studies alike that the environment in which a galaxy resides plays a pivotal role in the physical processes it undergoes and how its properties evolve over cosmic time (A. Von Der Linden et al. 2007; H. E. Loparelo et al. 2015; F. S. Liu et al. 2008; Y. Yoon et al. 2017; W. Van Kempen et al. 2024). Many stellar and kinematic properties of massive central galaxies, in addition to their morphology (S. M. Weinmann et al. 2006;

D. Zhao et al. 2015a; J. Cougo et al. 2020), are correlated with properties of the host system such as its size, mass, local galaxy number density (H. J. Martínez et al. 2013), and characteristics of its surrounding circumgalactic medium (V. Olivares et al. 2022; V. Saeedzadeh et al. 2023). For example, the stellar masses (D. Zhao et al. 2015b; K. E. Furnell et al. 2018; A. V. Kravtsov et al. 2018; S.-S. Li et al. 2025; S. I. Loubser 2019), star formation rates (SFRs; G. Gozaliasl et al. 2016), and radial stellar velocity dispersion (S. I. Loubser et al. 2018, 2022) of central galaxies are all correlated with the mass of their host haloes.

Group haloes are particularly interesting environments with which to test our galaxy formation models. BGGs and group galaxies in general have high vulnerability to mergers and tidal interactions (E. O'Sullivan et al. 2017; G. Gozaliasl et al. 2018, 2024; L. O. V. Edwards et al. 2020; B. D. Oppenheimer et al. 2021; S. L. Jung et al. 2022, and references therein) as a result of the high galaxy density and low velocity dispersion of group galaxies. The numerous interactions that BGGs experience over their lifetimes strongly influence the evolution of their properties. Galaxy-galaxy mergers, galactic cannibalism of small satellites (S. Shen et al. 2014), and cooling in the intragroup medium (IGrM) can cause influxes of gas to be funnelled inwards to the central BGG, providing fuel for star formation that contributes to building up its stellar mass and triggering AGN outbursts, as well as instigating kinematic, dynamic, and morphological transformations (S. I. Loubser et al. 2016; C. Nipoti 2017; K. Kolokythas et al. 2018, 2019; G. Gozaliasl et al. 2019; B. D. Oppenheimer et al. 2021; S. L. Jung et al. 2022; V. Saeedzadeh et al. 2023). As a consequence, BGGs are diverse and complex objects, with morphologies ranging from young, star-forming disc galaxies, to old, quenched spheroidal galaxies (S. M. Weinmann et al. 2006; G. Gozaliasl et al. 2016, 2025; S. I. Loubser et al. 2018, 2022; L. O. V. Edwards et al. 2020; K. Kolokythas et al. 2022; V. Olivares et al. 2022).

The diverse properties of BGGs have been found to be reflected in the ROMULUS simulations. A comprehensive analysis performed by S. L. Jung et al. (2022) showed that ROMULUS BGGs manifest with both disc and spheroidal morphologies. Case studies of specific group haloes, such as the ROMULUSG2 zoom-in simulation, revealed that rich histories of interactions and cycles of heating and cooling are responsible for moulding the BGGs' properties over cosmic time (S. L. Jung et al. 2022). From an observational perspective, G. Gozaliasl et al. (2016, 2018, 2024) have recently conducted a thorough investigation into the evolution of BGG properties

over cosmic time for BGGs belonging to X-ray-selected groups in the Cosmic Evolution Survey (COSMOS). In addition to a close examination of their BGGs' distributions in stellar mass and SFR, in a recent instalment, G. Gozaliasl et al. (2024) focused on the mass-weighted stellar ages of their BGGs, finding a positive correlation between stellar age and stellar mass, and a negative correlation between stellar age and SFR.

The complexity of BGGs' histories and the high correlation between their stellar and environmental properties make BGGs the perfect test bed for assessing how well our galaxy formation models describe distinct pathways of galaxy evolution like those seen in group environments. Several recent studies (e.g. J. Schaye et al. 2015; C. Nipoti 2017; A. Pillepich et al. 2018a; C. Ragona-Figueroa et al. 2018; N. A. Henden et al. 2020; T. M. Jackson et al. 2020) have examined massive central galaxies in cosmological simulations, including those residing in groups; however, few other than S. L. Jung et al. (2022) have focused solely on the evolution of simulated central galaxies on the group scale.

In this paper, we perform a detailed investigation into the stellar properties of populations of BGGs in the ROMULUS (M. Tremmel et al. 2017, 2019), SIMBA (R. Davé et al. 2019), SIMBA-C (R. T. Hough et al. 2023), and OBSIDIAN (D. Rennehan et al. 2024) simulation suites, focusing on their stellar mass, SFR, and stellar age distributions. In order to faithfully assess our simulated BGGs, we compare our results with a sample of COSMOS2020 BGG observations (J. R. Weaver et al. 2022) curated via cross-matching with a subset of the X-ray-selected group galaxies from G. Gozaliasl et al. (2016, 2018, 2019, 2020, 2024).

Descriptions of the simulations and their subgrid models can be found in Section 2 of this paper, with the COSMOS observations and the selection criteria used to extract populations of BGGs detailed in Section 3. In Section 4, we present the stellar properties and scaling relations of the simulated BGGs and compare them to our sample of observations. We discuss which simulations and associated subgrid physics prescriptions produce the most realistic results in Section 5, and summarise how successfully our galaxy formation models replicate BGGs and their group environments in Section 6.

2. SIMULATION METHODOLOGY

2.1. The ROMULUS Simulations

The ROMULUS suite consists of four smooth particle hydrodynamic (SPH) cosmological simulations: ROMULUS25, a $(25 \text{ cMpc})^3$ periodic volume, and three zoom-in simulations of individual group-scale systems ROMU-

LUSC, ROMULUSG1, and ROMULUSG2. All four ROMULUS simulations were run to $z = 0$ using the CHANGA Tree+SPH code (H. Menon et al. 2015) and comprise the same hydrodynamics, resolution, background cosmology, and subgrid physics (M. Tremmel et al. 2017, 2019). The ROMULUS background cosmology corresponds to a Λ CDM universe with parameters $\Omega_m = 0.309$, $\Omega_\Lambda = 0.691$, $\Omega_b = 0.0486$, $H_0 = 67.8 \text{ km s}^{-1} \text{ Mpc}^{-1}$, and $\sigma_8 = 0.82$, consistent with the results of P. a. R. Ade et al. (2016).

We refer readers to a number of previously published papers that have thoroughly described the ROMULUS simulations' hydrodynamics code and galaxy formation model: M. Tremmel et al. (2015, 2017, 2019, 2020); S. L. Jung et al. (2022); V. Saeedzadeh et al. (2023, 2024a,b), and references therein. Here, we summarise unique aspects of the ROMULUS simulations and their subgrid physics prescriptions that set them apart from the rest of the simulations we analyse.

A notable characteristic of the ROMULUS simulations is their high resolution, having dark matter and gas particles masses of $3.39 \times 10^5 \text{ M}_\odot$ and $2.12 \times 10^5 \text{ M}_\odot$ respectively, a Plummer equivalent gravitational force softening of 250 pc, and a maximum SPH resolution of 70 pc (M. Tremmel et al. 2017).

Stars in ROMULUS are formed stochastically in regions of dense ($n \geq 0.2 \text{ cm}^{-3}$) and cold ($T \leq 10^4 \text{ K}$) gas, assuming a P. Kroupa (2001) initial mass function (IMF). Star formation is regulated through the 'blastwave' (G. Stinson et al. 2006) implementation of type II supernovae (SNeII) feedback, which injects thermal energy into the interstellar medium (ISM) and temporarily disables cooling to prevent radiative losses.

The regulation of star formation within massive ROMULUS galaxies occurs in part due to feedback from their SMBHs. ROMULUS SMBHs are seeded based on local gas properties rather than simply imposing a minimum halo mass threshold as employed by many other simulations (e.g. I. G. McCarthy et al. 2017; N. A. Henden et al. 2018; A. Pillepich et al. 2018a). This ensures that SMBHs are formed in a physically motivated manner, from gas that is collapsing without fragmenting (M. Tremmel et al. 2017). An additional feature of ROMULUS SMBHs is that they are not artificially confined to the potential minimum of their halo, and instead undergo realistic orbital decay. This dynamical evolution of the SMBHs is tracked down to sub-kpc scales by means of the subgrid implementation of unresolved dynamical friction (M. Tremmel et al. 2015).

The SMBHs grow through mergers and a modified Bondi-Hoyle accretion prescription (H. Bondi 1952) that accounts for the angular momentum support of gas near

the SMBHs. ROMULUS employs a purely thermal SMBH feedback model where, at every SMBH timestep, a fraction (0.2%) of the rest mass energy of the accreting material is injected isotropically into the nearest 32 gas particles.

Free parameters of the ROMULUS subgrid models were systematically optimised to reproduce four important empirical scaling relations: stellar mass-halo mass (SMHM), SMBH mass-stellar mass, HI mass-stellar mass, and bulge-to-total ratio versus specific angular momentum (M. Tremmel et al. 2017, 2020; S. L. Jung et al. 2022).

2.2. The SIMBA Simulation

We utilise the flagship run of the SIMBA¹¹ simulation suite, which is a $(100 \text{ cMpc} h^{-1})^3$ cosmological volume containing 1024^3 dark matter particles and 1024^3 gas particles, that is run to $z = 0$ using the meshless finite mass (MFM) mode of the GIZMO N -body gravity+hydrodynamics solver (P. F. Hopkins 2015, 2017). The resolution of the simulation is detailed by dark matter and gas particles masses of $9.6 \times 10^7 M_\odot$ and $1.82 \times 10^7 M_\odot$ respectively, and a minimum Plummer-equivalent gravitational softening length of $0.5 h^{-1} \text{ kpc}$. The SIMBA background cosmology corresponds to a Planck 2018 (N. Aghanim et al. 2020) flat Λ CDM universe with parameters $\Omega_m = 0.3$, $\Omega_\Lambda = 0.7$, $\Omega_b = 0.048$, and $H_0 = 68 \text{ km s}^{-1} \text{ Mpc}^{-1}$.

We summarise fundamental aspects of the SIMBA simulation and its integrated subgrid physics prescriptions, and refer interested readers to R. Davé et al. (2016, 2019, 2020); A. Padawer-Blatt et al. (2025), and references therein, for more detailed descriptions of the simulation's underlying physics and methodology.

SIMBA assumes a G. Chabrier (2003) IMF, and employs a star formation model that is contingent on the density of H₂ gas, where H₂ fractions are determined following M. R. Krumholz & N. Y. Gnedin (2011) and the efficiency of star formation is $\epsilon_* = 0.02$ (R. Kennicutt 1998). Stellar feedback is implemented in SIMBA as decoupled, two-phase, metal-enriched SNe winds, with photoionisation heating and radiative cooling from the GRACKLE-3.1 library (B. D. Smith et al. 2017). The ISM is enriched by nine metals via an instantaneous recycling approximation (R. J. Talbot & W. D. Arnett 1971), wherein gas elements eligible to form stars are self-enriched by SNeII and SNeIa nucleosynthesis products prior to being transformed into a star particle. SNeIa and asymptotic giant branch (AGB) stars additionally release mass, energy, and metals through a

delayed feedback component (see R. Davé et al. 2016; A. Padawer-Blatt et al. 2025, for further detail). SIMBA also incorporates a dust formation, growth, and destruction model.

Black holes are seeded in SIMBA galaxies once the latter become resolved, with ~ 100 particles and $M_* \gtrsim 3 \times 10^9 M_\odot$. In contrast to the ROMULUS simulations, SIMBA SMBHs are pinned to the centre of their host galaxy. The black holes grow through a two-mode accretion model combining Bondi and torque-limited accretion (P. F. Hopkins & E. Quataert 2011; D. Anglés-Alcázar et al. 2017a). The latter accounts for the inflow of cold ($T < 10^5 \text{ K}$) gas resulting from the outward transport of angular momentum due to unresolved galactic-scale gravitational torques induced by non-axisymmetric perturbations in the stellar gravitational potential.

SIMBA employs a kinetic SMBH feedback subgrid model wherein bipolar gas outflows, which are hydrodynamically decoupled from their environment, are ejected from near the SMBH and recoupled after time $10^{-4} t_H$, where t_H is the Hubble time at launch (R. Davé et al. 2019). The feedback is divided into two regimes based on the Eddington ratio between the accretion rate of gas onto the SMBH and the Eddington accretion rate: $f_{\text{Edd}} = \dot{M}_{\text{acc}} / \dot{M}_{\text{Edd}}$. At high accretion rates ($f_{\text{Edd}} \gtrsim 0.22$), feedback takes the form of ISM-temperature ($\sim 10^4 \text{ K}$; R. Davé et al. 2019) radiative AGN winds, with ejection velocity dependent on the mass of the SMBH. Jet mode is activated at low accretion rates ($f_{\text{Edd}} \lesssim 0.22$) and for SMBHs above a minimum mass threshold. This threshold is defined as a range $M_{\text{BH}} \in [4 \times 10^7, 6 \times 10^7] M_\odot$, within which, the probability of jet activation increases with M_{BH} . In jet mode, gas is ejected at the halo's virial temperature with velocity equal to that of the radiative winds, but with an additional contribution inversely proportional to f_{Edd} . The jet component of the ejection velocity reaches a maximum of 7000 km s^{-1} at $f_{\text{Edd}} \leq 0.02$. Galaxies with low gas fractions additionally release X-ray feedback while in jet mode following the model of E. Choi et al. (2012).

The various subgrid models of the SIMBA simulation were calibrated to reproduce the $z = 0$ galaxy stellar mass function (GSMF), SMBH mass-stellar mass relation, and quenched galaxy fractions.

2.3. The SIMBA-C Simulation

SIMBA-C (R. T. Hough et al. 2023, 2024) is a variant of SIMBA that integrates the Chem5 stellar feedback and chemical enrichment model (C. Kobayashi et al. 2020a,b) into the galaxy formation model of R.

¹¹ <http://simba.roe.ac.uk/>

Davé et al. (2019). We employ the flagship run of the SIMBA-C simulation suite, which is a $(100 \text{ cMpc } h^{-1})^3$ cosmological volume comprising the same hydrodynamics, resolution, and background cosmology as the flagship SIMBA simulation discussed in Section 2.2.

Thorough discussions regarding the physics behind the 5 model and its integration into the SIMBA simulation can be found in the following papers: C. Kobayashi et al. (2020a,b); R. T. Hough et al. (2023, 2024). We summarise distinct characteristics of the SIMBA-C simulation arising from the updated implementation of stellar feedback and chemical enrichment. A detailed comparative summary of SIMBA and SIMBA-C can additionally be found in Section 2.1 of A. Padawer-Blatt et al. (2025).

SIMBA-C employs the same H_2 -based star formation model as SIMBA, but with a star formation efficiency of $\epsilon = 0.026$ (R. Pokhrel et al. 2021). The 5 model tracks all elements from H to Ge, and removes the instantaneous recycling approximation and delayed feedback. Following their formation, star particles eject mass, energy, and metals determined by 5 to reflect an evolving stellar population. The wind velocity scaling of the stellar winds is reduced to nearly half of that in SIMBA.

Black holes are seeded in SIMBA-C once galaxies reach a resolved stellar mass of $M_* \gtrsim 6 \times 10^8 \text{ M}_\odot$. The Bondi and torque-limited accretion model is preserved, but initial accretion rates for $M_{\text{BH}} < 3 \times 10^6 \text{ M}_\odot$ are suppressed so as to replicate the suppression of black hole growth by stellar feedback in dwarf galaxies (M. Habouzit et al. 2017; D. Anglés-Alcázar et al. 2017b; P. F. Hopkins et al. 2022). The range of SMBH masses at which the jet feedback mode is activated is shifted upward to $M_{\text{BH}} \in [7 \times 10^7, 10^8] \text{ M}_\odot$ in SIMBA-C. The maximum magnitude of the ejection velocity's jet component scales with the mass of the SMBH, and is capped at $35\,000 \text{ km s}^{-1}$.

Consistent with the calibration of the SIMBA simulation, free parameters of the SIMBA-C subgrid models were tuned to reproduce the $z = 0$ GSMF, SMBH mass-stellar mass relation, and quenched galaxy fractions.

2.4. The OBSIDIAN Simulation

The OBSIDIAN simulation is a new variant of SIMBA, with the addition of the OBSIDIAN black hole feedback subgrid model, introduced by D. Rennehan et al. (2024). The new subgrid model is implemented into a $(100 \text{ cMpc } h^{-1})^3$ cosmological volume simulation, which possesses the same hydrodynamics, resolution, and background cosmology as the flagship runs of SIMBA and SIMBA-C, and uses the same galaxy formation model

as SIMBA (R. Davé et al. 2019), but with the original SMBH feedback model replaced by the OBSIDIAN model. While most standard AGN feedback prescriptions model one or two distinct modes of feedback, OBSIDIAN is novel in that it is one of the first to incorporate three feedback regimes informed by more sophisticated subgrid accretion flow physics. More recently, S. Koudmani et al. (2024) and F. Huško et al. (2025) have proposed comparable models.

OBSIDIAN's three regimes of black hole feedback are partitioned based on the Eddington ratio, and model feedback of distinct accretion flow geometries (D. Rennehan et al. 2024). Mass from accreting gas is transferred to the SMBH corresponding to a regime-dependent growth rate, and the remaining mass is ejected at constant velocity as decoupled feedback. Variation in the SMBH outflows between regimes is primarily driven by the manner in which the accretion flow geometry impacts radiative efficiency. We summarise the three feedback regimes, and direct readers towards D. Rennehan et al. (2024) for a more comprehensive discussion of the physics that motivates the OBSIDIAN model.

High accretion rates ($f_{\text{Edd}} > 0.3$) correspond to the slim disc regime, which simulates feedback from a geometrically and optically thick accretion disc. Following A. Lupi et al. (2016), the slim disc radiative efficiency is dependent on the accretion rate and the spin of a SMBH, such that the efficiency decreases with increasing accretion rate and spin.

When the accretion rate is lowered to the range $0.03 \leq f_{\text{Edd}} \leq 0.3$, the SMBH enters the quasar regime, which mimics an efficiently radiating accretion disc that is geometrically thin, optically thick, and in local thermal equilibrium. The energetics of quasar mode are treated identically to slim disc mode, but with a radiative efficiency that depends only on SMBH spin.

At low accretion rates ($f_{\text{Edd}} \leq 0.03$) and for masses $M_{\text{BH}} \geq 5 \times 10^7 \text{ M}_\odot$, SMBHs are in the advection-dominated accretion flow (ADAF) regime, where the accretion disc is hot, geometrically thick, and optically thin. The accretion flow is low-density and unable to cool rapidly, and thus radiates inefficiently, causing much of the accretion energy to be advected into the SMBH. In addition to powerful winds (A. J. Benson & A. Babul 2009), ADAF mode incorporates large-scale jets that are launched isotropically via magnetic field lines entwining and extracting energy from a rotating SMBH. Following R. Y. Talbot et al. (2021), the efficiency of the jet is dependent on the spin of the SMBH, as well as the magnetic flux and the scale height of the

flow close to the SMBH's horizon. The jets are ejected at a constant velocity of $10\,000\,\text{km}\,\text{s}^{-1}$.

The OBSIDIAN simulation subgrid models were calibrated to reproduce the GSMF, the SMBH mass-stellar mass relation, and the quenched galaxy density at $z = 2$.

2.5. Calculating Simulated BGG Properties

ROMULUS haloes and subhaloes were identified using Amiga Halo Finder (AHF; S. R. Knollmann & A. Knebe 2009), and tracked across timesteps using TANGOS (A. Pontzen & M. Tremmel 2018). AHF locates peaks in the simulations' density fields and identifies all particles (dark matter, gas, stars, and black holes) gravitationally bound to each peak, constructing a nested hierarchy of haloes and subhaloes by finding successively larger structures (V. Saeedzadeh et al. 2023). In the SIMBA, SIMBA-C, and OBSIDIAN simulations, galaxies and haloes were identified, analysed, and tracked across timesteps using the CAESAR¹² Python package. CAESAR uses a friends-of-friends (FOF) algorithm to identify galaxies as groups of cold gas and stars, and links them to associated groups of dark matter that make up their host haloes.

We note that the differing methods used to identify group haloes in the ROMULUS and SIMBA-based simulations have no significant impact on the results presented in Section 4. A. Knebe et al. (2011) compare the properties of haloes derived from a number of halo finders, and find good agreement between haloes identified by AHF and FOF-based methods, including in the number of halo particles and the M_{200} halo mass. The M_Δ halo mass is defined as the total mass of a halo's gravitationally bound particles enclosed within a sphere of radius R_Δ centred on the halo's potential minimum, such that the sphere's mean interior density is Δ times the critical cosmological density (ρ_{crit} ; see, for example, A. Babul et al. 2002). Some deviation was found between the AHF and FOF halo centres due to the latter using the centre-of-mass, rather than the potential minimum (A. Knebe et al. 2011); however, the FOF algorithm of CAESAR, which we use, adopts the minimum potential halo centre, thus placing all of our simulated group haloes on equal footing (D. Rennehan 2024). To select samples of simulated BGGs in Section 3.2, we utilise the group haloes' IGrM X-ray luminosities, but otherwise exclusively analyse properties of the BGGs themselves.

X-ray luminosities of the simulated haloes are summed from the individual luminosities of hot ($T > 5 \times 10^5\,\text{K}$) and diffuse gas particles within R_{500} of the haloes' potential minima. We note that the appropriate density

threshold for defining the IGrM depends on details of the simulation, including its mass resolution, density threshold for star-formation, and how its hydrodynamic solver and subgrid models affect the presence and distribution of gas phases in galaxies and their haloes (M. S. Peeples et al. 2019; F. van de Voort et al. 2019; S. Appleby et al. 2023). The ROMULUS IGrM is defined by the density threshold $\rho < 500\rho_{\text{crit}}$, which was arrived at empirically as that which selects all hot diffuse halo gas, while excluding the ISM and other dense substructure (M. Tremmel et al. 2019). For the SIMBA-based simulations, we adopt the conventional IGrM density threshold $n_{\text{H}} < 0.13\,\text{cm}^{-3}$ (below the threshold for star formation; R. T. Hough et al. 2024; A. Padawer-Blatt et al. 2025), and additionally exclude hydrodynamically decoupled stellar and AGN wind particles, as their properties are not tracked while decoupled from the surrounding gas (F. Jennings & R. Davé 2023).

We opt to use independent definitions for IGrM density in the ROMULUS and SIMBA-based simulations, as each simulation's conventional threshold was derived such that the relationship between halo mass and IGrM temperature ($M-T$) generally follows that observed (see M. Tremmel et al. 2019; R. T. Hough et al. 2024). We verify that with their respective density thresholds, the simulations' $M-T$ relations are comparable and also agree with the observed relation.

We explicitly test the impact of applying the ROMULUS IGrM density criterion to the SIMBA-based simulations and find no significant difference in the resulting IGrM X-ray luminosities compared to those computed using the conventional $n_{\text{H}} < 0.13\,\text{cm}^{-3}$ threshold. We additionally find that within each simulation, the calculated group X-ray luminosities are insensitive to the choice of temperature threshold within the range $T \in [2 \times 10^5, 10^6]\,\text{K}$. Given this robustness, we adopt the conventional density criterion for the SIMBA-based simulations for consistency with the broader literature, while retaining the $\rho < 500\rho_{\text{crit}}$ definition for ROMULUS, and use a temperature threshold of $T > 5 \times 10^5\,\text{K}$ for all simulations.

The particle X-ray luminosities are calculated by XI-GrM¹³ using X-ray spectra generated by PyAtomDB (A. Foster et al. 2016; A. R. Foster & K. Heuer 2020; A. R. Foster et al. 2021) for combined continuum, and metallicity-dependent line emission in the $0.1-2.4\,\text{keV}$ energy band. We excise the inner $0.15R_{500}$ core to avoid contamination from possible cool cores as well as very hot gas, present due to the adopted AGN feedback pre-

¹² <https://caesar.readthedocs.io/>

¹³ <https://xigrm.readthedocs.io/>

scription (see L. Liang et al. 2016; M. Tremmel et al. 2019; R. T. Hough et al. 2024; A. Padawer-Blatt et al. 2025, for further detail). Cylindrical apertures are conventional for comparing to X-ray observations made in projection; however, for all simulations, we find a median relative difference of $< 15\%$ between core-excised X-ray luminosities within spherical and cylindrical apertures. The choice of aperture does not significantly impact the results presented in Section 4, and we thus opt to use a core-excised spherical shell of radius R_{500} for simplicity.

The stellar properties of BGGs in the SIMBA-based simulations are calculated using CAESAR, which directly identifies particles belonging to each galaxy. The BGGs' stellar masses are given by the sum of the masses of their associated star particles. SFRs are determined by the mass of stars formed during the 100 Myr period immediately preceding the snapshot of interest, and stellar ages are the mass-weighted stellar age (Age_w) of all the BGGs' stars.

We identify the centres of ROMULUS BGGs by applying the shrinking spheres approach (C. Power et al. 2003) to the gravitationally bound star particles of their host haloes. Properties of ROMULUS galaxies are calculated within apertures, typically spherical or cylindrical in shape (B. D. Oppenheimer et al. 2021; S. L. Jung et al. 2022). Within the BGGs' apertures, stellar masses are calculated as the sum of the star particle masses, SFRs are the mass of stars formed during the time elapsed between the snapshot of interest and its predecessor, and stellar ages are the stellar mass-weighted average age of all the stars within the aperture.

As a consequence of the small simulation volume, our sample of ROMULUS BGGs (described in detail in Section 3.2) occupy a narrow distribution in both mass and size, meaning that all BGGs' stellar properties can be reasonably described by a constant aperture size. V. Saeedzadeh et al. (2023) demonstrate that the radii of ROMULUS BGGs, defined as 4 times the half-mass radius (Z. Hafem et al. 2019), do not exceed 30 kpc. We find the ROMULUS BGG stellar properties to be consistent within 10% between spherical and cylindrical apertures of radius 30 kpc, as well as between spherical apertures of radius 30 kpc and 50 kpc. We therefore calculate the ROMULUS BGGs' stellar properties within radii of $r = 30$ kpc about their centres, using spherical apertures to replicate the FOF-based galaxy identification of CAESAR. We additionally verify that for the SIMBA-based simulations, there is a median relative difference of $\lesssim 10\%$ between the stellar properties calculated using CAESAR and those calculated within a sphere of radius $r = 30$ kpc.

3. COMPARISON TO OBSERVATIONS

3.1. The COSMOS Sample

To assess how reliably our simulations can replicate real BGGs in the universe, we compare the stellar properties of simulated BGGs to those of BGGs sampled from a catalogue of X-ray-selected groups in the COSMOS field. The COSMOS groups were initially identified as extended X-ray sources by A. Finoguenov et al. (2007) using combined *Chandra* and *XMM-Newton* data, with group members identified via multiband photometry. The catalogue was later revised by G. Gozaliasl et al. (2019) to include spectroscopic observations. We refer readers to A. Finoguenov et al. (2007, 2009, 2010, 2015); M. R. George et al. (2011); G. Gozaliasl et al. (2014, 2019), for detailed discussions regarding the methodology used to identify and analyse the COSMOS X-ray groups.

Spectroscopic redshifts were determined for COSMOS groups with at least 3 group members with spectroscopic data, and photometric redshifts were measured otherwise, following the methodology described by G. Gozaliasl et al. (2019). The groups were assigned quality flags, which characterise the integrity of their X-ray emission and the reliability of their optical counterparts (G. Gozaliasl et al. 2014, 2019; G. Toni et al. 2024). To perform a robust comparison to the simulations, we restrict our COSMOS sample to high-quality groups with spectroscopically determined redshifts and X-ray quality flags of 1 or 2. Flag 1 describes groups with unique X-ray centres and optical counterparts, and flag 2, groups that share X-ray emission with another object in projection but are otherwise distinct and well-defined.

The COSMOS BGGs presented in G. Gozaliasl et al. (2016, 2018, 2019, 2020, 2024) were identified as the most massive and luminous member residing within R_{200} of each group's X-ray centre. In the present study, we focus on low-redshift systems and utilise a subset of these BGGs occupying the redshift range $z \in [0.08, 0.38]$, with core-excised group X-ray luminosities $\log(L_{\text{X}}/\text{erg s}^{-1}) \gtrsim 41.4$ measured within R_{500} in the 0.1–2.4 keV energy band. Physical properties of the BGGs were obtained from the COSMOS2020 catalogue (J. R. Weaver et al. 2022).

The COSMOS2020 catalogue was constructed from multi-wavelength photometry performed on 1.7 million sources detected in the COSMOS field (J. R. Weaver et al. 2022). We utilise COSMOS2020 stellar masses and star formation rates that were determined using the LePhare code (S. Arnouts et al. 2002; O. Ilbert et al. 2006), which fits spectral energy distributions (SEDS) to the galaxies' observed photometry. Stellar masses

are derived following the methodology of O. Ilbert et al. (2015), assuming a G. Chabrier (2003) IMF, and with templates generated using the G. Bruzual & S. Charlot (2003) Stellar Population Synthesis (SPS) model (C. Laigle et al. 2016). The mass-weighted stellar ages of the BGGs were determined following S. Wuys et al. (2011); see also, G. Gozaliasl et al. (2024). The COSMOS2020 galaxy properties assume a standard Λ CDM cosmology with parameters $\Omega_m = 0.3$, $\Omega_\Lambda = 0.7$, and $H_0 = 70 \text{ km s}^{-1} \text{Mpc}^{-1}$.

3.2. Samples of Simulated BGGs

COSMOS, ROMULUS, and the three variants of the SIMBA simulation adopt Λ CDM cosmologies with three different values of H_0 : COSMOS with $H_0 = 70 \text{ km s}^{-1} \text{Mpc}^{-1}$, ROMULUS with $H_0 = 67.8 \text{ km s}^{-1} \text{Mpc}^{-1}$, and the SIMBA-based simulations with $H_0 = 68 \text{ km s}^{-1} \text{Mpc}^{-1}$. Upon extracting BGGs from the simulations, we convert their physical properties, following the scaling described by D. J. Croton (2013), to the background cosmology of the COSMOS2020 catalogue. Henceforth, the properties of all BGGs we analyse and discuss correspond to a Λ CDM universe with $H_0 = 70 \text{ km s}^{-1} \text{Mpc}^{-1}$.

As shown in Figure 1, the COSMOS BGGs (grey diamonds) fall in three main concentrations in redshift. Correspondingly, we divide the $z \in [0.08, 0.38]$ redshift range of the COSMOS sample into three bins of equal size: $z \in [0.08, 0.18]$, $z \in [0.18, 0.28]$, and $z \in [0.28, 0.38]$. In each redshift bin, we extract the physical properties of BGGs in simulated galaxy groups from three sequential simulation snapshots spanning the redshifts of the highest density of COSMOS BGGs, giving a total of nine snapshots. Galaxy groups are identified as haloes that contain at least 3 ‘luminous’ galaxies¹⁴ with stellar mass greater than 10% of that of the least massive BGG in the COSMOS sample.

To perform a reasonable comparison between like populations of simulated and observed BGGs, we require that the simulated groups have the same minimum core-excised X-ray luminosity as the COSMOS groups ($\log(L_{X, 0.1-2.4 \text{ keV}}/\text{erg s}^{-1}) \gtrsim 41.4$), as well as comparable redshift distributions. The simulation samples are constructed via a differential evolution algorithm (R. Storn & K. Price 1997), which selects each BGG from one of the nine snapshots such that the two-sample Kolmogorov-Smirnov (KS) statistic between the COSMOS and simulation cumulative redshift distributions

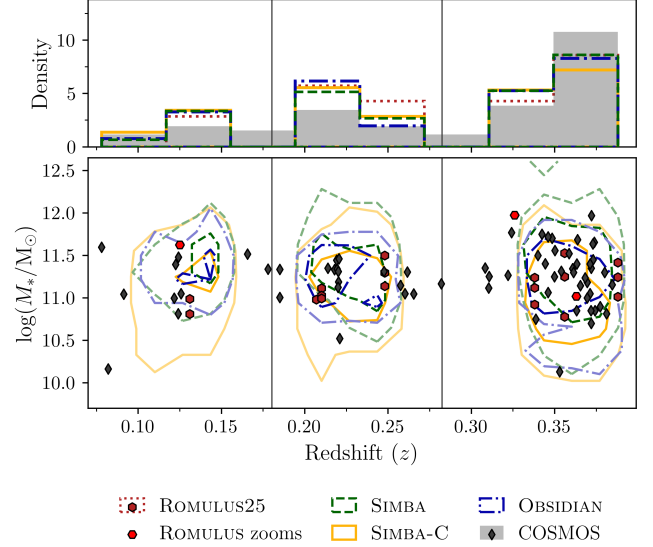


Figure 1. **Top:** BGG redshift distributions. Simulated BGGs satisfying $\log(L_{X, 0.1-2.4 \text{ keV}}/\text{erg s}^{-1}) \geq 41.4$ are selected from nine snapshots to match the redshift distribution of the COSMOS sample (grey shaded histogram). The ROMULUS25 histogram is outlined in dotted red, SIMBA in dashed green, SIMBA-C in solid yellow, and OBSIDIAN in dot-dashed blue. The vertical black lines mark the boundaries between redshift bins $z \in [0.08, 0.18]$, $z \in [0.18, 0.28]$, and $z \in [0.28, 0.38]$. **Bottom:** BGG stellar mass as a function of redshift. COSMOS BGGs are shown as grey diamonds, ROMULUS25 BGGs as dark red hexagons, and BGGs from the ROMULUS zoom simulations as bright red hexagons. The SIMBA, SIMBA-C, and OBSIDIAN BGGs are represented by 1σ and 3σ 2D histogram contour lines.

is minimised, and each galaxy only appears once in the final sample.

Figure 1 depicts the resulting redshift distributions of the simulated BGGs as histograms in the top panel, and on the stellar mass-redshift plane in the bottom panel. The ROMULUS25 BGGs are shown as dark red hexagons, and the SIMBA, SIMBA-C, and OBSIDIAN BGGs are represented by 1σ and 3σ 2D histogram contour lines in green, yellow, and blue, respectively. BGGs from the ROMULUS zoom simulations, ROMULUSC, ROMULUSG1, and ROMULUSG2, are not included in the ROMULUS25 redshift distribution, but are shown on the stellar mass-redshift plane as bright red hexagons.

The $L_X - M_*$ relations for the BGG samples prior to the X-ray luminosity cut are shown in the top panel of Figure 2. The SIMBA, SIMBA-C, and OBSIDIAN BGGs are represented by median lines, with outer lines and data points respectively illustrating the 16th and 84th interpercentile regions and the systems beyond. All other formatting follows that of Figure 1. The bottom panel of Figure 2 has the $L_X - M_*$ relations for BGGs from groups

¹⁴ In the SIMBA-based simulations, this is equivalent to requiring at least 3 galaxies with ≥ 64 star particles (R. T. Hough et al. 2024).

Table 1. The number of BGGs with $\log(L_{X, 0.1-2.4\text{keV}}/\text{erg s}^{-1}) \gtrsim 41.4$ per total sample, and within two equal-sized stellar mass bins: $\log(M_*/M_\odot) \in [9.88, 11.23]$ and $\log(M_*/M_\odot) \in [11.23, 12.57]$.

Stellar Mass	ROMULUS	SIMBA	SIMBA-C	OBSIDIAN	COSMOS
$\log(M_*/M_\odot) < 11.23$	12	90	287	90	28
$\log(M_*/M_\odot) \gtrsim 11.23$	9	140	163	106	39
Total	21	230	450	196	67

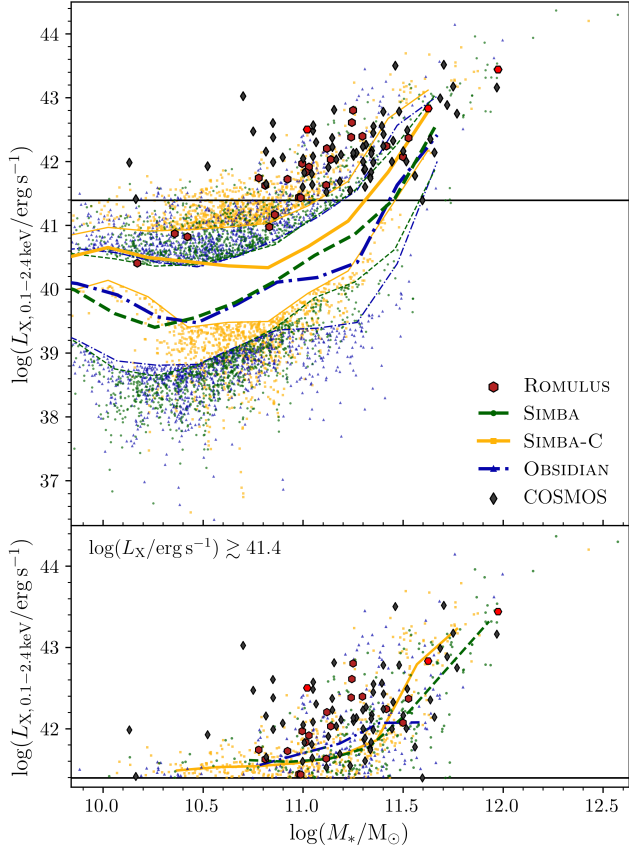


Figure 2. $L_X - M_*$ relations for observed and simulated BGGs. **Top:** The initial samples of simulated BGGs for all L_X . The SIMBA, SIMBA-C, and OBSIDIAN BGGs are represented by median lines, with outer lines and data points showing the 16th and 84th inter-percentile regions and outer scatter. The black line illustrates the COSMOS minimum $\log(L_{X, 0.1-2.4\text{keV}}/\text{erg s}^{-1}) \simeq 41.4$. All other formatting follows that of Figure 1. **Bottom:** The selected samples satisfying $\log(L_X/\text{erg s}^{-1}) \gtrsim 41.4$. All SIMBA, SIMBA-C, and OBSIDIAN BGGs are shown as data points in addition to their medians.

with $\log(L_{X, 0.1-2.4\text{keV}}/\text{erg s}^{-1}) \gtrsim 41.4$, where we depict all BGGs of the large-volume simulations in addition to their median lines. Given that all our X-ray luminosities are measured in the $0.1-2.4\text{keV}$ energy band, we hereafter shorten $L_{X, 0.1-2.4\text{keV}}$ to L_X .

We select the simulation samples based on X-ray luminosity to mirror the COSMOS group catalogue, which is X-ray-selected and therefore limited to systems with de-

tectable IGrM X-ray emission. Because the IGrM X-ray luminosity scales with halo mass, this selection intrinsically favours more massive, gas-rich haloes, while lower-mass, X-ray-dim systems are more likely to fall below the detection threshold. Given that the properties and evolution of BGGs are closely coupled to the thermodynamic state and mass of their host haloes, restricting the simulation samples to groups above the COSMOS detection threshold ensures a like-to-like comparison with the COSMOS BGG population.

The number of selected BGGs with $\log(L_X/\text{erg s}^{-1}) \gtrsim 41.4$ within the COSMOS and simulation samples is summarised in Table 1, where we further divide the BGGs into two equal-sized stellar mass bins, $\log(M_*/M_\odot) \in [9.88, 11.23]$ and $\log(M_*/M_\odot) \in [11.23, 12.57]$, for analysis in Section 4.

4. BRIGHTEST GROUP GALAXIES

In this section, we present the stellar properties of BGGs from the ROMULUS, SIMBA, SIMBA-C, and OBSIDIAN simulations, and compare them to the sample of observed COSMOS BGGs. We investigate the BGGs' stellar masses, SFRs, and stellar ages in Section 4.1, and explore scaling relations of their stellar properties in Section 4.2.

4.1. Stellar Property Distributions

We make use of two-sample KS tests to quantitatively compare the stellar property distributions of simulated BGGs to those of COSMOS. Following standard practice in astronomy (e.g. M. Cowles & C. Davis 1982; A. Babul 1991; M. Caleb et al. 2019; T. Kuutma et al. 2020; G. Gozaliasl et al. 2025), we require a significance level of 5%, meaning a p -value lower than 0.05, to reject the null hypothesis that there is no difference between the two distributions being considered. We do, however, acknowledge the systematic differences in how stellar properties are derived between simulations and observations, including assumptions about the mass function of stars within the central galaxies, when interpreting KS p -values close to the threshold of 0.05. Finally, we emphasise that, as shown in Table 1, the BGG samples are not all of equal size and ROMULUS has a significantly smaller sample size than the other simulations.

4.1.1. Stellar Mass

The stellar masses of the simulated and observed BGGs are displayed in Figure 3 as 1D normalised density histograms. The median stellar mass of each sample is indicated by a vertical line corresponding in colour to the sample's histogram curve. ROMULUS25 is shown in red (dotted median), SIMBA in green (dashed median), SIMBA-C in yellow (solid median), and OBSIDIAN in blue (dot-dashed median). The simulations' distributions are contrasted against that of the COSMOS sample, represented by the grey shaded curve and solid grey median line. Due to the small sample size, we do not include a distribution for the ROMULUS zoom simulations, and instead show their individual stellar masses as bright red hexagons in the bottom panel of Figure 3. The table in Figure 3 contains the results of two-sided KS tests comparing the $\log(M_*/M_\odot)$ distributions of the simulated BGG samples to that of the COSMOS sample.

The ROMULUS25 BGGs occupy a narrow range in $\log(M_*/M_\odot)$ in comparison to the other samples. The small (25 cMpc^3) simulation volume constrains both the number of systems that can form and how massive they will become. This limits the extent of the high- M_* end of the distribution. As seen in Figure 2, the ROMULUS simulations boast higher X-ray luminosities for a given stellar mass than the median relations of SIMBA and its variants, due in part to thermal AGN feedback being inefficient at expelling hot gas from haloes (B. D. Oppenheimer et al. 2021). This results in ROMULUS25 having a low median stellar mass, with $\sim 61\%$ of the sample composed of low-mass BGGs with $\log(M_*/M_\odot) < 11.23$ that exceed the minimum L_X threshold. The ROMULUS25 stellar mass distribution is formally inconsistent with that of COSMOS at the 5% level of significance; however, with the KS test $p = 0.041$, this result may be affected by systematic differences in the measurement of stellar mass between the two samples.

SIMBA-C has the lowest median stellar mass and is the only sample excluding ROMULUS25 that predominantly contains BGGs in the low- M_* bin (see Table 1). Similarly to ROMULUS25, this is due to SIMBA-C generally having greater X-ray luminosities for a given stellar mass than the SIMBA or OBSIDIAN simulations, which results in a greater fraction of low- M_* SIMBA-C BGGs residing in haloes with $\log(L_X/\text{erg s}^{-1}) \gtrsim 41.4$. As discussed in R. T. Hough et al. (2024) and A. Padawer-Blatt et al. (2025), low-mass groups in SIMBA-C have higher X-ray luminosities than in SIMBA due to having greater masses of hot diffuse gas. This arises primarily from the delayed onset of AGN jet feedback in SIMBA-C, which we discuss further in Section 5. The SIMBA-C stellar mass distribu-

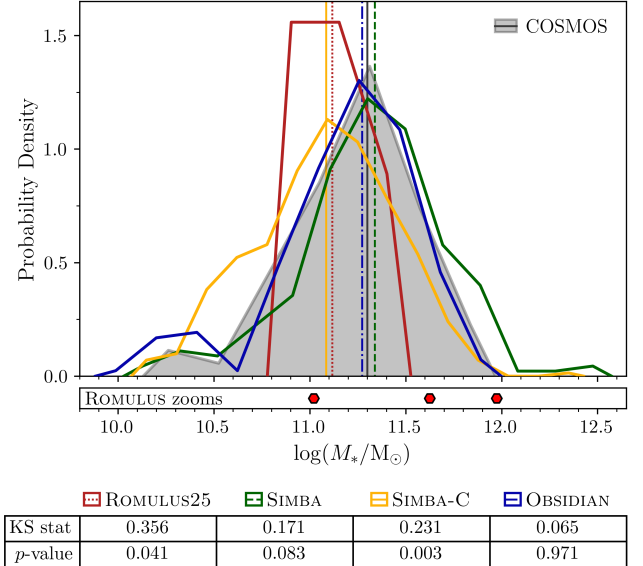


Figure 3. BGG stellar mass distributions illustrated by normalised density histograms. The solid curves and vertical lines of corresponding colour are the M_* distributions and sample medians respectively for the simulated BGG samples: ROMULUS25 (red, dotted median), SIMBA (green, dash-dotted median), SIMBA-C (yellow, solid median), and OBSIDIAN (blue, dashed median). COSMOS is represented by the grey shaded distribution and solid grey median line. BGG stellar masses from the ROMULUS zoom simulations are shown in the bottom panel as bright red hexagons. The table contains the results of two-sample KS tests comparing the simulations' $\log(M_*/M_\odot)$ distributions to that of COSMOS.

tion ($p = 0.003$) is incompatible with that of COSMOS at a 5% significance level.

In contrast to SIMBA-C, the SIMBA simulation has the largest median stellar mass and $p = 0.083$, which implies that the SIMBA and COSMOS stellar mass distributions are consistent with each other. In addition to having lower X-ray luminosities, which reduces the fraction of low- M_* BGGs above the L_X threshold, SIMBA contains an excess of high- M_* BGGs, including a handful of systems with $\log(M_*/M_\odot) \gtrsim 12$ that do not appear in the other samples. Jet feedback in SIMBA is capped at a significantly lower maximum velocity than SIMBA-C, and is thus less efficient at heating and ejecting gas from massive haloes. This allows BGGs in SIMBA to continue building up their stellar mass without sufficient suppression to their star formation (we discuss this further in Section 5.2).

The OBSIDIAN simulation boasts the highest level of agreement with COSMOS, having the closest distribution shape and median stellar mass, as well as a KS test result of $p = 0.971$, which implies that the two stellar mass distributions are compatible. Like SIMBA-

C, the OBSIDIAN model has been shown to produce higher hot gas fractions in low-mass groups compared to SIMBA (D. Rennehan et al. 2024), which gives OBSIDIAN a higher median X-ray luminosity for BGGs with $\log(M_*/M_\odot) < 10.5$ (see Figure 2, top panel). The OBSIDIAN median $\log(L_X/\text{erg s}^{-1})$ still falls $\gtrsim 0.5$ dex below that of SIMBA-C for $\log(M_*/M_\odot) \lesssim 10.8$, and as a result, the OBSIDIAN sample does not contain the excess of low- M_* systems found in SIMBA-C. The OBSIDIAN stellar mass distribution also does not exhibit the excess of high- M_* systems seen in that of SIMBA, nor the lack of such systems seen in SIMBA-C, suggesting that the OBSIDIAN AGN feedback model is more tempered when it comes to suppressing star formation in massive systems.

4.1.2. Specific Star Formation Rate

The measurement and calculation of sSFR is subjected to a minimum detection threshold as a consequence of the limited resolution of simulations (M. Donnari et al. 2019; K. G. Iyer et al. 2020; J. A. Flores Velázquez et al. 2021) and instrumentation sensitivities for observations (M. Fukugita & M. Kawasaki 2003; M. S. Bothwell et al. 2011; D. Calzetti 2013; C. Conroy 2013; M. Figueira et al. 2022). Given the established uncertainty in measuring observed star formation below $\log(\text{sSFR}/\text{yr}^{-1}) \sim -12$ (D. Schiminovich et al. 2007; L. K. Hunt et al. 2019), we follow the usual convention (see, for example R. Davé et al. 2019; B. D. Oppenheimer et al. 2021) and set all $\log(\text{sSFR}/\text{yr}^{-1}) \leq -12$ to the arbitrary value of $\log(\text{sSFR}/\text{yr}^{-1}) = -14$; representing BGGs with immeasurably low levels of star formation. This ensures that the distribution of measurable sSFRs contains only reliable values and that information about both simulated and observed BGGs with very low and potentially uncertain sSFR is not lost.

Figure 4 depicts the normalised density histograms and sample medians describing the sSFRs of our simulated and observed BGGs. The top panel of Figure 4 follows the same formatting as Figure 3, and the middle and bottom panels respectively show the sSFR distributions of the low and high stellar mass subsamples defined in Table 1. We note that the peaks at $\log(\text{sSFR}/\text{yr}^{-1}) = -14$ are artificial and represent each sample's proportion of BGGs with immeasurable sSFR, as the ‘true’ sSFRs of these galaxies are very low and highly uncertain. KS tests comparing the full distributions of sSFR are highly sensitive to this subset, and we opt to perform such statistical analyses on samples of sSFR whose values are measurable and whose distribution is meaningful. Figure 4 therefore tabulates the results of KS tests comparing each simulation's distri-

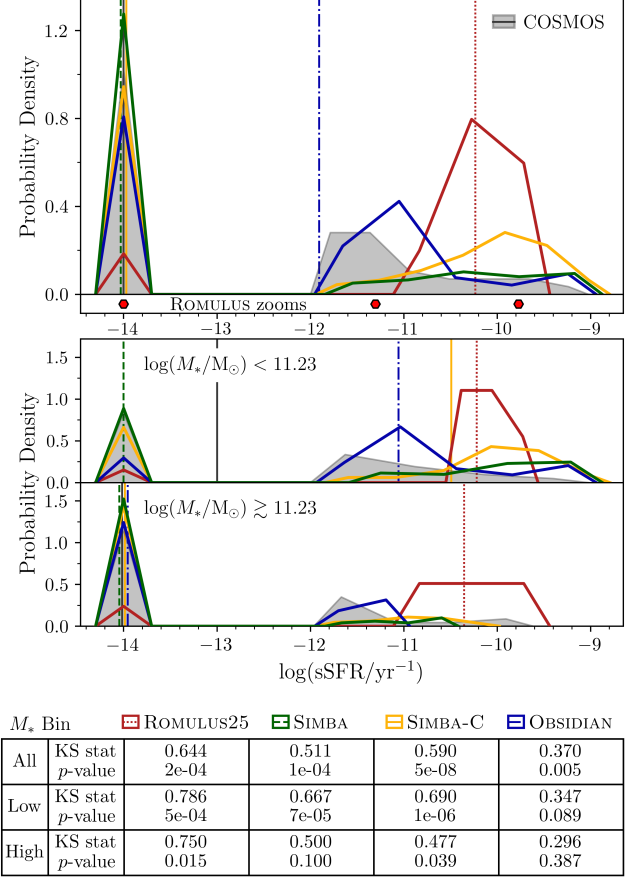


Figure 4. BGG sSFR distributions. The top panel depicts the full BGG samples, the middle panel shows BGGs in the low- M_* bin with $\log(M_*/M_\odot) < 11.23$, and in the bottom panel, BGGs in the high- M_* bin with $\log(M_*/M_\odot) \gtrsim 11.23$ (see Table 1). All BGGs with $\log(\text{sSFR}/\text{yr}^{-1}) \leq -12$ are set to $\log(\text{sSFR}/\text{yr}^{-1}) = -14$ to account for the minimum detection threshold of sSFR (see text). All other formatting follows that of Figure 3. The table contains the results of two-sided KS tests comparing the simulation samples' distributions of measurable $\log(\text{sSFR}/\text{yr}^{-1}) > -12$ to that of the COSMOS sample. The top, middle, and bottom rows respectively compare $\log(\text{sSFR}/\text{yr}^{-1}) > -12$ distributions in the full, low- M_* , and high- M_* samples.

bution of measurable $\log(\text{sSFR}/\text{yr}^{-1}) > -12$ to that of COSMOS, where the top row includes BGGs of all stellar masses, and the middle and bottom rows compare distributions in the low- and high- M_* subsamples respectively. We note that some BGGs with low, but measurable sSFR can still be considered as quenched, meaning that a sample's fraction of BGGs with immeasurable sSFR is not equal to its quenched fraction. We investigate the BGG quenched fractions in more detail in Section 4.2.

ROMULUS25 BGGs exhibit significantly heightened levels of star formation compared to the other samples,

having the highest median sSFR and the largest fraction of measurable sSFRs for all stellar masses. These results align with those of S. L. Jung et al. (2022), who find that ROMULUS BGGs have high levels of star formation, acquiring their cold, star-forming gas via satellite stripping or cooling in the IGrM (V. Saeedzadeh et al. 2023). Efficient cooling of the ROMULUS halo gas can explain the enhanced BGG star formation as well as the higher IGrM X-ray emission seen in Figure 2. The ROMULUS median ssSFR in the high- M_* bin is ~ 0.2 dex lower than in the low- M_* bin, but there is otherwise no strong sign of star formation being quenched in BGGs of greater stellar mass. The p -values in Figure 4 demonstrate that the ROMULUS25 measurable sSFR distributions are incompatible with those of COSMOS for all ranges of stellar mass.

In contrast to ROMULUS, COSMOS and the three large-volume simulations show strong evidence of increased quenching in massive BGGs, demonstrated by the reduced upper sSFR limits and heightened peaks in immeasurable sSFR within the high- M_* bin compared to the low- M_* bin. The SIMBA sample has the largest fraction of BGGs with immeasurably low sSFR in all stellar mass bins, and is the only simulation with $>50\%$ immeasurable sSFRs in the low- M_* bin. The measurable $\log(\text{sSFR}/\text{yr}^{-1}) > -12$ distribution of SIMBA is nearly flat, and is compatible with the measurable distribution of COSMOS only in the high- M_* bin, where $p = 0.1$.

For all ranges of stellar mass, the KS test results indicate that the COSMOS and SIMBA-C measurable sSFR distributions are formally incompatible at 5% significance. In the high- M_* bin, where the value $p = 0.039$ is close to the significance threshold, the rejection of the null hypothesis may be affected by differences in the sSFR measurements of SIMBA-C and COSMOS. The SIMBA-C sample contains a population of star-forming BGGs in the low- M_* bin that do not appear in COSMOS or the other variants of the SIMBA simulation. Whether this is a consequence of the SIMBA-C sample's greater proportion of low- M_* BGGs with $\log(L_X/\text{erg s}^{-1}) \gtrsim 41.4$, or a broader feature of BGG star formation in the SIMBA-C simulation, is explored further in Sections 4.2 and 5.2.

The OBSIDIAN sSFR distribution is in the greatest agreement with that of COSMOS. With $p = 0.005$, the measurable sSFR distributions of COSMOS and OBSIDIAN are incompatible for the full range of stellar mass; however, the KS tests reveal compatibility between the two distributions when split into the low ($p = 0.089$) and high ($p = 0.387$) stellar mass subsamples. The OBSIDIAN simulation has the only measurable sSFR distribution that matches the shape of COSMOS in that

the distribution rises towards lower sSFRs and peaks at $\log(\text{sSFR}/\text{yr}^{-1}) < -11$. An increasing fraction of galaxies in the transitional state between high and immeasurably low sSFR suggests that the COSMOS and OBSIDIAN BGG populations are undergoing a gradual quenching process, as opposed to a sudden drop in star formation. We further investigate evidence of slow versus fast quenching processes in Sections 4.2 and 5.

4.1.3. Stellar Age

The distributions of mass-weighted stellar age (Age_w) describing the age of the bulk of the BGGs' stars can be seen in Figure 5 following the same formatting as Figure 4. The table in Figure 5 contains the results of two-sided KS tests comparing each simulation's Age_w distributions to those of COSMOS, for the full samples in the top row, and the low- and high- M_* subsamples in the middle and bottom rows respectively.

As a consequence of the heightened star formation seen in Figure 4, the ROMULUS25 BGGs contain large populations of young stars, which shifts the median stellar age and distribution peak to lower ages in comparison to the other samples. The median stellar age of the ROMULUS25 BGGs is younger in the high- M_* bin than in the low- M_* bin, corroborating that star formation is under-regulated in massive BGGs (S. L. Jung et al. 2022). When divided into the low- M_* ($p = 0.074$) and high- M_* ($p = 0.050$) subsamples, the ROMULUS25 and COSMOS Age_w distributions are formally indistinguishable.

The population of low- M_* star-forming BGGs in SIMBA-C (see Figure 4) heightens the low-age tail of the Age_w distribution and gives SIMBA-C the lowest median stellar age in the low- M_* bin. Between the low- and high- M_* bins, however, the median increases by ~ 0.13 dex (corresponding to ~ 2 Gyr), which also gives SIMBA-C the largest median stellar age in the high- M_* bin. This points towards there being a greater distinction between the recent star formation histories of high and low stellar mass BGGs in SIMBA-C than seen in the other samples, driven by SIMBA-C's population of low- M_* star-forming BGGs. For all ranges of stellar mass, the SIMBA-C stellar age distributions are incompatible at 5% significance with those of COSMOS.

The OBSIDIAN simulation, despite having the greatest proportion of BGGs with measurable sSFR (excluding ROMULUS25), also has the highest median Age_w and distribution peak. Paired with the peak in low, but measurable sSFR in Figure 4, this suggests that the OBSIDIAN BGGs undergo a gradual decline in star formation, which prevents a large mass of newly formed stars from lowering the mass-weighted stellar age, even

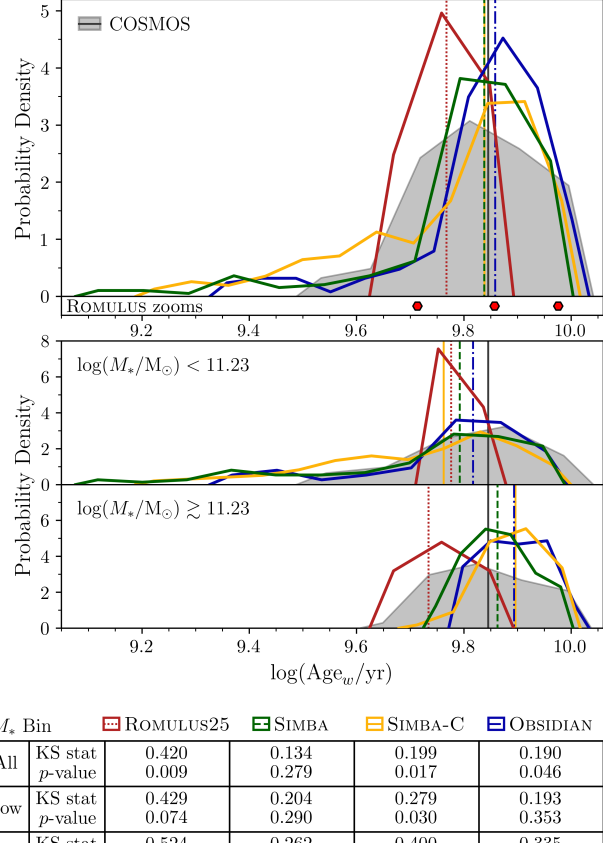


Figure 5. BGG mass-weighted stellar age (Age_w) distributions. Formatting follows that of Figure 4. The table contains the results of KS tests comparing the simulations’ $\log(\text{Age}_w/\text{yr})$ distribution to that of COSMOS, where the top, middle, and bottom rows respectively compare the full, low- M_* , and high- M_* samples.

while the BGGs continue forming stars at a measurable rate. The OBSIDIAN Age_w distribution is narrower than that of COSMOS in the high- M_* bin, and shifted to higher ages, resulting in the two samples’ Age_w distributions being formally indistinguishable only in the low- M_* subsample ($p = 0.353$). For the full stellar mass samples, however, the rejection of the null hypothesis may be influenced by differences in the measurement of Age_w between OBSIDIAN and COSMOS, as $p = 0.046$ comes close to the significance level of 5%.

With $p = 0.279$, the SIMBA simulation has the only Age_w distribution formally compatible with COSMOS for the full range of stellar masses. The two samples additionally have compatible low- M_* Age_w distributions ($p = 0.290$). In the high- M_* bin, the median and peak Age_w of SIMBA is closest to that of COSMOS and falls below the other large-volume simulations. A younger median stellar age in combination with the high fraction

of BGGs with immeasurably low sSFR seen in Figure 4 implies that massive BGGs in SIMBA may have been quenched more recently or quickly than those in SIMBA-C and OBSIDIAN, so as to possess both low sSFRs and younger stellar populations.

COSMOS has a consistent median stellar age for all stellar mass bins, and the high- Age_w bulk of the COSMOS BGGs have a wider distribution than all the simulations. This is most prominently seen in the high- M_* bin, where the extent of the low-age end of the distribution alludes to the presence of massive, actively star-forming BGGs in the COSMOS sample.

4.2. Stellar Property Scaling Relations

4.2.1. Star Formation and Quenching Relations

Figure 6 examines the sSFR– M_* relations for the samples of BGGs with measurable $\log(\text{sSFR}/\text{M}_\odot) > -12$. The central panel shows the BGGs as data points on the sSFR– M_* plane following the same formatting as Figure 2. The purple line represents the K. E. Whitaker et al. (2012) star-forming main sequence (SFMS) and the accompanying shaded region defines ± 0.75 dex about this relation. The top and right panels respectively show the stellar mass and sSFR distributions for the BGG samples with $\log(\text{sSFR}/\text{M}_\odot) > -12$. These distributions are normalised with respect to the number of galaxies with $\log(\text{sSFR}/\text{M}_\odot) > -12$ in each sample and otherwise follow the same formatting as Figures 3–5. The median sSFR and stellar mass corresponding to each sample on the distribution panels are extended onto the sSFR– M_* plane in the central panel. Following S. L. Jung et al. (2022), we define a BGG as quenched if it falls at least 0.75 dex below the K. E. Whitaker et al. (2012) SFMS, indicated by the black line in Figure 6.

Nearly all ROMULUS BGGs with $\log(\text{sSFR}/\text{M}_\odot) > -12$ are considered to be star-forming, with the exception of two ROMULUS25 BGGs and ROMULUSC that fall below the quenched line. All these star-forming BGGs are contained within the purple shaded region of Figure 6, closely following the K. E. Whitaker et al. (2012) SFMS. Star formation in the ROMULUS simulations is not sufficiently suppressed, causing the majority of ROMULUS BGGs to remain on the SFMS rather than beginning to quench as a population.

The large population of low- M_* BGGs with $\log(L_\text{X}/\text{erg s}^{-1}) \gtrsim 41.4$ seen in SIMBA-C’s stellar mass distribution (Figure 3) coincides with the sample’s peak in measurable sSFR in Figure 4. The majority of SIMBA-C BGGs with measurable sSFR fall on the K. E. Whitaker et al. (2012) SFMS and in the low- M_* bin with $\log(M_*/\text{M}_\odot) < 11.23$. Across all stellar masses, the SIMBA-C sample contains few BGGs with sSFRs that

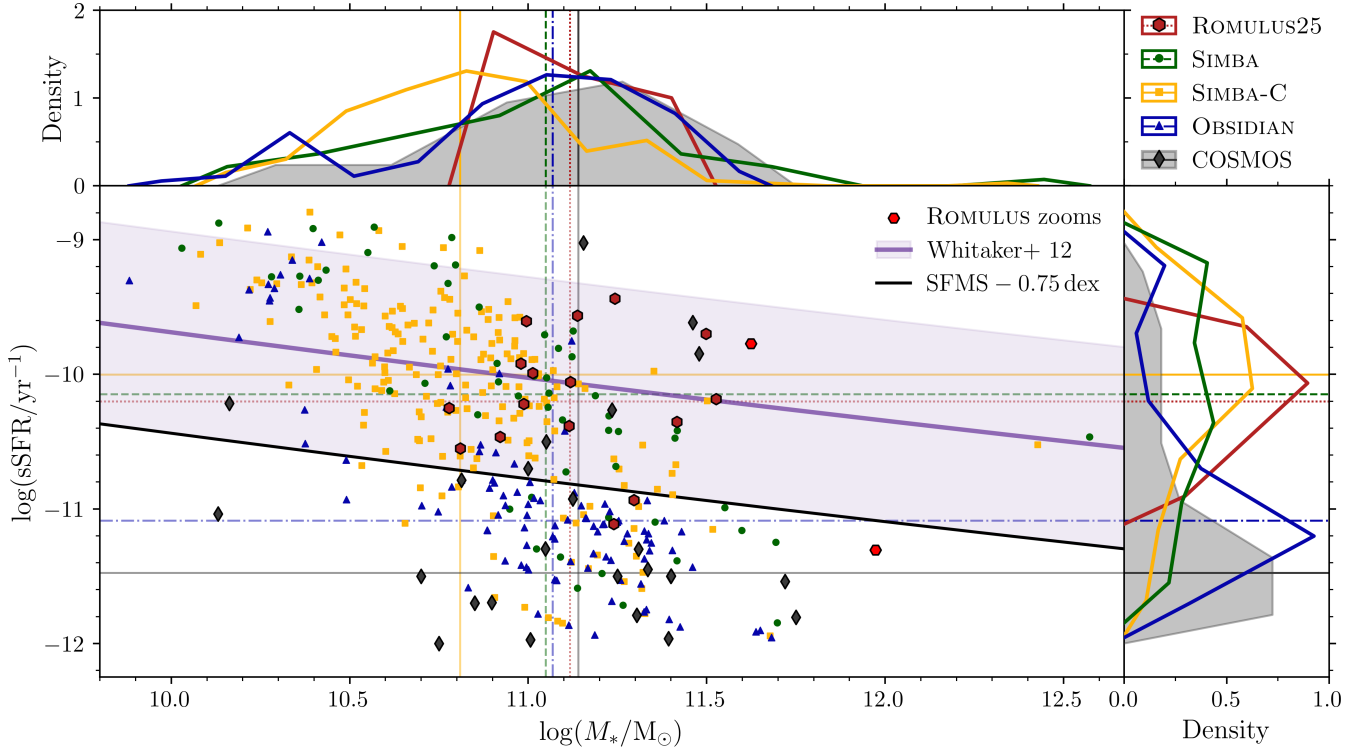


Figure 6. sSFR – M_* relations for samples of BGGs with $\log(\text{sSFR}/\text{yr}^{-1}) > -12$. The central panel depicts individual BGGs on the sSFR – M_* plane with markers following the formatting of Figure 2. The purple line is the K. E. Whitaker et al. (2012) SFMS, with the corresponding shaded band showing the region ± 0.75 dex around it. BGGs are considered quenched if they fall under the black line sitting 0.75 dex below the K. E. Whitaker et al. (2012) SFMS. The top and right panels respectively show the stellar mass and sSFR distributions for the samples of BGGs with $\log(\text{sSFR}/\text{yr}^{-1}) > -12$, normalised with respect to the measurable sSFR sample sizes and following the same formatting as Figures 3–5. The samples’ median stellar masses and sSFRs are shown as lines on the distributions and extended onto the central panel. BGGs from the ROMULUS zoom simulations are not included in the ROMULUS25 distributions, but are shown on the sSFR – M_* plane as bright red hexagons.

are both measurable and considered quenched. Comparatively, the SIMBA sample is more evenly distributed in sSFR, ranging from above the K. E. Whitaker et al. (2012) SFMS down to near the measurable sSFR limit. The SIMBA sample does not contain any BGGs with measurable but quenched sSFRs for $\log(M_*/M_\odot) \lesssim 11$, despite having a sizeable proportion of immeasurable sSFRs in this range (see Figure 4).

All three large-volume simulations have low- M_* , highly star-forming BGGs that are not present in the COSMOS sample. Both the COSMOS and OBSIDIAN stellar mass distributions have a local peak at $\log(M_*/M_\odot) \sim 10.3$. In OBSIDIAN, this peak is occupied by star-forming BGGs, but in COSMOS, it contains BGGs that are quenched or in the process of quenching. On the opposite end of the sSFR – M_* plane, there is a handful of high- M_* , star-forming BGGs in the COSMOS sample that lie in a region of the plane only otherwise inhabited by ROMULUS BGGs. Massive BGGs with recent star formation activity explains the low stellar ages

reached by the high- M_* Age_w distribution of COSMOS (see Figure 5).

The bulk of the OBSIDIAN and COSMOS samples are in good agreement on the sSFR – M_* plane, primarily concentrated between the lower end of the K. E. Whitaker et al. (2012) SFMS and the measurable sSFR limit. COSMOS and OBSIDIAN are the only samples whose measurable sSFR distributions are dominated by quenched galaxies.

The BGG quenched fractions are illustrated in Figure 7 as a function of stellar mass in the left panel and for the full samples in the overlaid bar plot on the right. The thick lines and star symbols show the relative quenched fractions in stellar mass bins of width 0.25 dex, with their estimated uncertainty depicted by the associated shaded regions. The thin lines and error bars respectively represent the cumulative quenched fractions as a function of stellar mass and their uncertainty. The quenched fractions include all BGGs with immeasurable sSFR and those with measurable sSFR

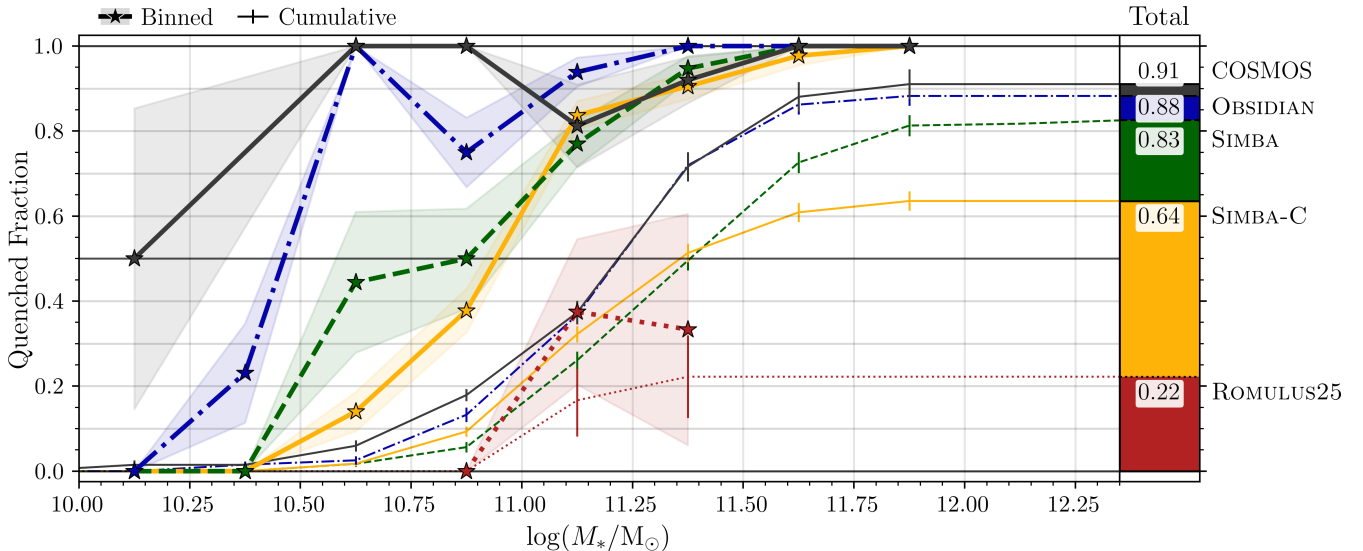


Figure 7. BGG quenched fractions. BGGs are considered quenched if they lie more than 0.75 dex below the K. E. Whitaker et al. (2012) SFMS (see Figure 6). The thick lines and star symbols show the relative quenched fractions in stellar mass bins of width 0.25 dex that contain ≥ 2 BGGs, with the associated shaded regions depicting the fractions’ estimated uncertainty. The thin lines and error bars respectively represent the cumulative quenched fractions and their uncertainty as a function of stellar mass. Each sample’s total BGG quenched fraction is illustrated by the overlaid bar plot on the right. COSMOS fractions are shown in grey, ROMULUS25 in red, SIMBA in green, SIMBA-C in yellow, and OBSIDIAN in blue.

falling at least 0.75 dex below the K. E. Whitaker et al. (2012) SFMS.

The inefficient suppression of star formation in the ROMULUS simulations is apparent in Figure 7, where no individual mass bin exceeds 40% quenched and only 22% of all ROMULUS25 BGGs are quenched. Next to ROMULUS25, SIMBA-C has the lowest total quenched fraction (64%) due to the contribution from the population of low- M_* star-forming BGGs. The SIMBA-C relative quenched fraction gradually steepens with stellar mass, climbing to $\gtrsim 80\%$ at $\log(M_*/M_\odot) \sim 11$. Contrastingly, SIMBA’s relative quenched fraction abruptly rises from 0% to nearly 50% between the bins crossing $\log(M_*/M_\odot) = 10.5$. This, and SIMBA’s higher total quenched fraction of 83% can be linked to jet feedback activating in less massive SMBHs and consequently, less massive galaxies.

OBSIDIAN’s total quenched fraction of 88% comes closest to that of COSMOS (91%). The relative quenched fractions of the two samples differ at low stellar masses owing to the low- M_* star-forming OBSIDIAN BGGs seen in Figure 6. For $\log(M_*/M_\odot) \gtrsim 10.5$, however, both the COSMOS and OBSIDIAN BGGs consistently fall between 75% and 100% quenched. The cumulative quenched fractions of OBSIDIAN and COSMOS diverge for both the highest and lowest stellar masses, where there are fewer galaxies and weaker statistics, but strongly agree for intermediate mass BGGs. Of the

large-volume simulations, OBSIDIAN simultaneously has the lowest fraction of BGGs with immeasurable sSFR (see Figure 4) and the highest quenched fraction across all stellar masses.

4.2.2. Stellar Age Relations

How the BGGs’ mass-weighted stellar age scales with other stellar properties can provide insight into the recent evolution of their stellar populations. Figure 8 presents the BGG samples’ Age_w as a function of stellar mass in the top panel and sSFR in the bottom panel. All formatting follows that of Figure 2.

There is overlap between the ROMULUS and COSMOS stellar ages as a function of stellar mass. Most ROMULUS BGGs align with the lower- Age_w end of the COSMOS sample and fall below the median relations of the large-volume simulations due to the presence of young stellar populations. The COSMOS sample contains a few outlying BGGs with low stellar masses and high stellar ages corresponding with the low- M_* quenched BGGs seen in Figure 6.

The large-volume simulations display the same general trend in Age_w as a function of stellar mass, in that Age_w rises steeply for low stellar masses and flattens for $\log(M_*/M_\odot) \gtrsim 11$. This trend signifies the growing mass of young stars in low- M_* BGGs as they build up their mass, followed by the ageing and lack of replenishment of these stars as high- M_* BGGs begin quenching. The steep, low- M_* end of this trend is not obviously

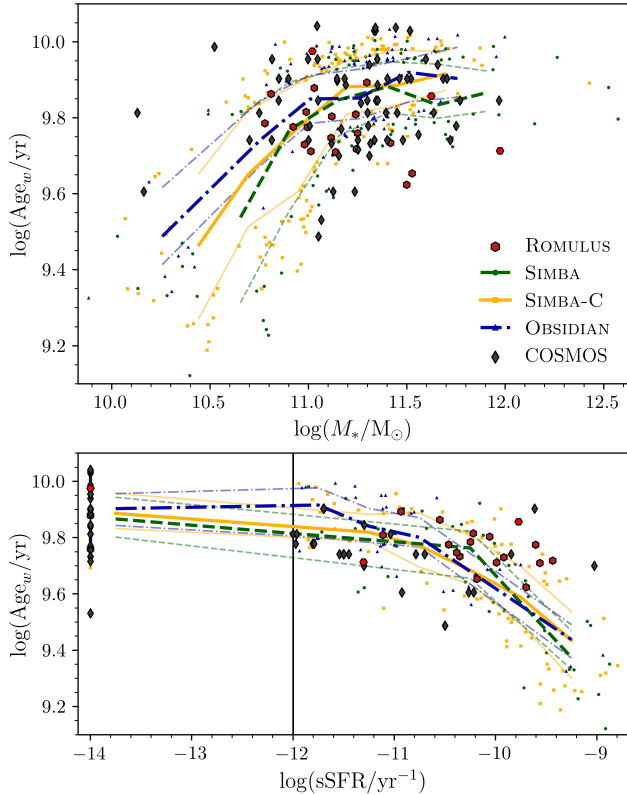


Figure 8. BGG stellar age scaling relations. The BGG mass-weighted stellar age (Age_w) is shown as a function of stellar mass in the top panel, and as a function of sSFR in the bottom panel. All formatting follows that of Figure 2. The vertical black line in the bottom panel represents the measurable $\log(\text{sSFR}/\text{yr}^{-1}) > -12$ limit.

present in the ROMULUS or COSMOS samples, which lack significant statistics in that area.

In the bottom panel of Figure 8, the Age_w of the large-volume simulations follow a compatible trend as a function of sSFR, where star-forming BGGs have large masses of young stars, and as sSFR decreases, fewer new stars are formed and the existing stellar populations age. The ROMULUS and COSMOS samples again do not exhibit the same low- Age_w trend due to having few low- M_* systems. BGGs' stellar mass is built up over time, so young stellar populations present in massive star-forming BGGs would typically make a lesser contribution to the mass-weighted stellar age than those in less massive BGGs. Because of this, the ROMULUS and COSMOS Age_w –sSFR relations are flatter than those of the large-volume simulations, which have significantly more low- M_* systems. The high- M_* , star-forming BGGs seen in the ROMULUS and COSMOS samples in Figure 6 manifest in the Age_w –sSFR plane as the BGGs with $\log(\text{sSFR}/\text{yr}^{-1}) \sim -9.5$ sitting at or above the upper Age_w scatter of the large-volume simulations.

Despite following the same general trends, there are variations in the Age_w scaling relations of the large-volume simulations, corroborating that their BGG populations are following different evolutionary paths. OBSIDIAN has the shallowest $\text{Age}_w - M_*$ slope as well as the highest median Age_w for nearly the full range in stellar mass. This means that OBSIDIAN BGGs are, on average, both older and ageing slower compared to BGGs of similar mass in the SIMBA and SIMBA-C simulations. The contrasting lower median ages and steeper $\text{Age}_w - M_*$ slopes of SIMBA-C and in particular, SIMBA, represent BGGs with higher proportions of young, more recently formed stars that age quickly due to a lack of replenishment from continued star formation. At $\log(M_*/M_\odot) \gtrsim 11.4$, the SIMBA median Age_w declines, signalling a recent rise in star formation in high- M_* BGGs that could be the cause of the excess of massive systems seen in SIMBA's stellar mass distribution (Figure 3). This is also reflected in the Age_w –sSFR relation, where SIMBA BGGs with $\log(\text{sSFR}/\text{yr}^{-1}) \sim -10.2$ have the highest median Age_w due to the presence of massive systems with ageing stellar populations that continue to form new stars.

The median Age_w of all the large-volume simulations rises with decreasing sSFR, but for $\log(\text{sSFR}/\text{yr}^{-1}) \lesssim -10.8$, as star formation begins to slow and quench, the SIMBA and SIMBA-C median Age_w flattens while OBSIDIAN's continues to rise. At the measurable limit of $\log(\text{sSFR}/\text{yr}^{-1}) = -12$, OBSIDIAN's median Age_w is ~ 1.7 Gyr higher than those of SIMBA and SIMBA-C. This is indicative of slow versus fast quenching processes. When SIMBA and SIMBA-C BGGs become quenched, they contain higher proportions of young stars, which can be explained by recent star formation that has suddenly been suppressed. In OBSIDIAN, a gradual decline in star formation can allow the BGGs to advance in age while still forming stars at a measurable rate, resulting in BGGs hosting older stellar populations upon reaching immeasurable levels of star formation.

5. DISCUSSION

In this section, we review the results presented in Section 4 and examine in further detail how the subgrid prescriptions employed by each simulation affect characteristics of their BGG populations. We summarise how closely each simulation's results reflect those of the observed COSMOS BGGs in Section 5.1, and in Section 5.2, we investigate what drives the differences in BGG populations seen across simulations and what this suggests about the evolutionary processes they experience.

5.1. Agreement with COSMOS Observations

The properties of simulated BGGs presented in Section 4 display varying levels of agreement with observations. While we have aligned our model results with the COSMOS group catalogue’s BGG measurements, redshift distribution, and cosmology, direct comparisons between simulated and observed galaxy properties are subject to inherent systematic variations. This context is relevant when reviewing the following overview of the simulations’ agreement with COSMOS.

In the case of ROMULUS25, a caveat to the comparison with COSMOS lies in the small $(25 \text{ cMpc})^3$ simulation volume, which limits the number and mass of groups and their central BGGs that can form. ROMULUSC, whose stellar mass is ~ 0.45 dex larger than the most massive ROMULUS25 BGG, had its initial conditions extracted from a $(50 \text{ cMpc})^3$ cosmological volume. This is reported by [M. Tremmel et al. \(2019\)](#) to be the minimum volume within which groups the size of ROMULUSC can form. The ROMULUS zoom simulations cannot contribute to a statistical comparison between BGG populations, but do provide a reference for how BGGs in massive systems evolve under the ROMULUS galaxy formation model.

The most significant disagreement between the ROMULUS and COSMOS samples is in the former’s high rates of BGG star formation. Across all stellar masses, the ROMULUS sample is dominated by star-forming BGGs and has a considerably smaller fraction of immeasurably low sSFRs than COSMOS. When isolating measurable sSFRs in Figure 6, the ROMULUS25 median stellar mass is in closest agreement with that of COSMOS; however, the star formation within these BGGs is highly different. The vast majority of ROMULUS systems are contained within ± 0.75 dex of the [K. E. Whitaker et al. \(2012\)](#) SFMS, while most COSMOS BGGs fall below this and are considered quenched.

A point of agreement between ROMULUS and COSMOS is in the presence of highly star-forming BGGs with $\log(M_*/M_\odot) \sim 11.5$, which do not appear in the other simulation samples. Recent star formation causes these BGGs to have lower mass-weighted stellar ages than quenched systems of similar mass, which contributes to stellar age being the only property of ROMULUS25 deemed compatible with COSMOS through the metric of two-sample KS tests. High- M_* , star-forming BGGs are consistent with broader characteristics of the ROMULUS sample, but the handful of such BGGs that appear in COSMOS are outliers to the sample’s trend of star formation suppression and quenching in massive systems.

A common area where the large-volume simulations disagree with observations occurs at low stellar masses,

where COSMOS lacks statistically significant representation. BGGs with $\log(M_*/M_\odot) \lesssim 10.5$ from SIMBA and its variants are predominantly star-forming, and highly so, mainly located within or above the upper $+0.75$ dex region around the [K. E. Whitaker et al. \(2012\)](#) SFMS (see Figure 6). Contrastingly, the few galaxies with such masses in the COSMOS sample have suppressed or quenched sSFRs.

These low- M_* portions of the samples being dominated by BGGs sitting above the SFMS implies a correlation at low stellar masses between highly star-forming BGGs and those in the upper scatter of the $L_X - M_*$ relation that surpass the minimum X-ray luminosity threshold $\log(L_X/\text{erg s}^{-1}) \gtrsim 41.4$. In simulations, increased star formation and X-ray luminosity can both be linked to cooling in the IGrM. Hot diffuse IGrM gas emits in X-ray as it cools, and this cooled gas can be funnelled towards the central BGG and provide fuel for star formation.

This also explains much of the disagreement seen between the SIMBA-C and COSMOS samples. Low-mass groups in SIMBA-C have greater masses of hot diffuse gas than in SIMBA ([R. T. Hough et al. 2024](#); [A. Padawer-Blatt et al. 2025](#)), resulting in greater X-ray luminosities, which pushes a larger proportion of BGGs with $\log(M_*/M_\odot) \lesssim 10.8$ above the minimum L_X threshold and into the BGG sample. In connection with the cooling of their hot IGrM gas, these excess low- M_* BGGs are also predominantly star-forming. This causes the SIMBA-C sample to contain a large population of BGGs with low stellar masses, high sSFRs, and low stellar ages that disagree with the COSMOS sample. The two-sample KS tests further demonstrate that all SIMBA-C stellar property distributions are incompatible with those of COSMOS.

BGGs from the SIMBA simulation are more consistent with the COSMOS observations than those from SIMBA-C. With lower masses of hot diffuse gas leading to lower group X-ray luminosities, the SIMBA sample does not contain the excess of low- M_* star-forming systems seen in SIMBA-C. SIMBA does however, produce massive systems with $\log(M_*/M_\odot) \gtrsim 12$ that do not appear in COSMOS. Despite this, the median stellar mass of SIMBA is close to that of COSMOS, and the stellar mass distributions of the two samples are compatible.

The measurable sSFR distribution of SIMBA is virtually flat with a slight peak on the [K. E. Whitaker et al. \(2012\)](#) SFMS, which contrasts with the bulk of COSMOS’ measurable sSFRs being classified as quenched for all stellar masses. The SIMBA and COSMOS measurable sSFR distributions are compatible only in the high- M_* bin where SIMBA BGGs no longer follow the

SFMS. SIMBA has a higher fraction of BGGs with immeasurable sSFR than COSMOS, but lacks COSMOS' significant presence of systems transitioning from high to immeasurable sSFRs. This signals a fundamental difference in the quenching processes experienced by the two BGG populations. Despite this disagreement in sSFR, SIMBA and COSMOS have compatible distributions of stellar age.

The OBSIDIAN simulation has the highest overall agreement with COSMOS. The results of the KS tests show that OBSIDIAN and COSMOS have compatible distributions of stellar mass, measurable sSFR, and stellar age for low- M_* BGGs. OBSIDIAN's stellar mass distribution does not contain the excess of low- M_* BGGs seen in SIMBA-C nor the highly massive systems present in SIMBA, and closely matches the shape, peak, and median of the COSMOS distribution.

The most significant consistency between OBSIDIAN and COSMOS, where all other simulations fall short, is in the BGGs' star formation characteristics. OBSIDIAN is the only simulation whose measurable sSFR distribution, like that of COSMOS, peaks below the K. E. Whitaker et al. (2012) SFMS. The presence of BGGs transitioning from high to immeasurable sSFRs results in the two samples having the closest quenched fractions, as a function of stellar mass and in total, and gives strong evidence that the two BGG populations are following similar evolutionary paths. The sSFR– M_* plane in Figure 6 and the quenched fraction in Figure 7 additionally show that the quenching processes taking place in OBSIDIAN and COSMOS BGGs begin at lower stellar masses than in the other simulations. Efficient and steady regulation of star formation at all stellar masses likely also drives the close agreement between the OBSIDIAN and COSMOS stellar mass distributions.

These results paint a picture of a gradual quenching process, where the BGG population experiences a slow decline in sSFR as a function of mass rather than a sudden halt to all star formation once a critical mass scale is reached. BGGs produced by the OBSIDIAN simulation not only have global properties aligning with those of COSMOS observations, but also undergo physical processes that allow them to grow and evolve as a population in a manner resembling the evolution of real massive galaxies.

5.2. The Impact of Subgrid Prescriptions

5.2.1. Thermal AGN Feedback

Apart from limitations arising from the small simulation volume, the primary distinction between ROMULUS and the other samples considered here is the excessive

star formation among ROMULUS BGGs and the inefficient quenching of massive galaxies.

The quenching of massive central galaxies generally hinges on the suppression of their fuel source from one or a combination of two factors: the removal of hot gas from the halo, and the prevention of this gas from forming cooling flows that can condense onto the galaxy. It has been established that the heightened star formation and low quenched fractions among ROMULUS BGGs originate in the inefficiency of its thermal AGN feedback in suppressing cooling flows (B. D. Oppenheimer et al. 2021; S. L. Jung et al. 2022).

Evidence of over-cooling in ROMULUS groups has been discussed by S. L. Jung et al. (2022) and V. Saeedzadeh et al. (2023). In the results of Section 4, this can be seen in the high sSFRs of the ROMULUS BGGs and in their higher core-excised X-ray luminosities compared to the other simulations (see Figure 2).

Thermal AGN feedback in ROMULUS occurs at every SMBH timestep, where 0.2% of the rest mass energy of accreting material is injected into the nearest 32 gas particles (M. Tremmel et al. 2017). This added energy, however, does not affect the gas on large enough spatial scales or long enough timescales to prevent cooling flows from fuelling BGG star formation. A suspected cause for this is that gas near the SMBH, after receiving thermal energy, is immediately able to cool and radiate much of this energy away before having the chance to interact with surrounding particles and drive large-scale heating and outflows.

Similar problems arose in early implementations of thermal stellar feedback, where added energy was radiated away too quickly to allow for the formation of stellar-driven winds (R. S. Somerville & R. Davé 2015). Several techniques were developed to address this issue, one of which is utilised by the G. Stinson et al. (2006) ‘blastwave’ stellar feedback model implemented in the ROMULUS simulations. In this model, gas particles that receive thermal energy from stellar feedback have their radiative cooling turned off for the predicted duration of a SN wind. Thermal AGN feedback in ROMULUS does not employ such a technique (S. L. Jung et al. 2022). Gas particles heated by SMBHs are not prevented from cooling, so their thermal energy may be radiated away before they are able to significantly influence their surroundings.

The EAGLE cosmological simulation (J. Schaye et al. 2015; R. A. Crain et al. 2015), which also employs a purely thermal AGN feedback model, prevents immediate radiative losses by releasing energy stored by the SMBH in discrete bursts that heat gas particles to high temperatures ($\Delta T = 10^9$ K) to mitigate overcool-

ing (C. M. Booth & J. Schaye 2009). At fixed stellar mass, EAGLE produces higher BGG quenched fractions than ROMULUS (see Figure 9 of B. D. Oppenheimer et al. 2021), and exhibits rising quenched fractions with increasing mass. However, these fractions remain lower than both observed BGG quenched fractions and those produced by simulations incorporating kinetic AGN feedback (R. Davé et al. 2020; S. L. Jung et al. 2022; M. Einasto et al. 2024). This suggests that, even with measures in place to prevent radiative losses, thermal feedback alone is insufficient at quenching star formation in massive systems.

At the simplest level, AGN feedback is understood to be a dominant factor suppressing the growth of massive galaxies in the group regime, making the choice of feedback model critical for realistically modelling group environments and their central galaxies. Inefficient AGN feedback drives ROMULUS’ disagreement with observed stellar properties of BGGs and impacts the underlying evolutionary processes that shape these global properties.

5.2.2. High-Temperature Metal-Line Cooling

In group-scale haloes, hot gas is primarily cooled through metal-line emission. In simulations, however, incorporating metal-line cooling across all temperatures has been shown to lead to excessive gas overcooling within galaxies when molecular hydrogen physics is unresolved (C. R. Christensen et al. 2014). Motivated by these findings, the ROMULUS simulations include only low-temperature ($T \leq 10^4$ K) metal cooling (see S. L. Jung et al. 2022, Section 2.1 for a detailed discussion on this matter). While the exclusion of high-temperature metal-line cooling may appear inconsistent with the overcooling in massive ROMULUS haloes, this choice is supported by earlier work demonstrating that the inclusion of full metal cooling results in large, high-entropy cores in groups and clusters, and conversely, the exclusion of high-temperature metal cooling leads to low-entropy cool-cores (Y. Dubois et al. 2011). Enhanced metal cooling can increase gas inflow onto the central SMBH, accelerating black hole growth and triggering more energetic AGN feedback events, which, if efficiently coupled to the surrounding gas, can create entropy cores and suppress further cooling. Realistically modelling high-temperature metal-line cooling therefore requires consideration of its dependencies on commonly unresolved processes, such as molecular hydrogen and dust physics, as well as its complex, non-linear interactions with existing subgrid models, including chemical enrichment, and stellar and AGN feedback (see Y. Ni

et al. 2023, for a discussion of the complex dependencies involving AGN feedback).

5.2.3. Kinetic AGN Feedback

Distinctive BGG characteristics produced by the SIMBA-C simulation are potentially due to three major changes made to the SIMBA galaxy formation model: the addition of the 5 treatment of chemical enrichment, reduced stellar wind velocity scaling, and AGN jet feedback that is onset at higher SMBH masses and can reach higher maximum velocities.

The higher X-ray luminosities responsible for the excess of low- M_* , star-forming BGGs in the SIMBA-C sample are *not* a consequence of the increased number of elements tracked by the 5 model. R. T. Hough et al. (2023, 2024) and A. Padawer-Blatt et al. (2025) found that groups of a given halo mass in SIMBA-C generally have lower metal mass fractions than those of similar mass in SIMBA. In isolation, lower metal mass fractions would reduce X-ray emission due to metal-line cooling and result in lower X-ray luminosities. The higher X-ray luminosities seen in Figure 2 thus originate from SIMBA-C’s higher masses of hot diffuse gas in low-mass groups.

These higher masses of hot gas can be attributed to less efficient feedback. In group-scale haloes, the dominant mechanism for removing hot halo gas is AGN feedback, and AGN jets in SIMBA-C are only activated in massive systems. However, in lower-mass groups with shallower gravitational potential wells, stellar feedback can also contribute to gas expulsion (L. Liang et al. 2016), meaning that the reduced stellar wind velocity scaling of SIMBA-C could also be a contributing factor.

Implementation of the three-regime model of black hole feedback was the only change made to the SIMBA galaxy formation model in the creation of the OBSIDIAN simulation. No non-AGN subgrid model parameters were recalibrated (D. Rennehan et al. 2024). All differences found in the BGG populations of SIMBA and OBSIDIAN are therefore solely a result of changes to the SMBH feedback, and the signatures of each simulation’s distinct feedback model are reflected in the properties of the BGGs they produce.

In Figure 9, we take a detailed look at the star formation and quenching processes affecting BGGs in SIMBA, SIMBA-C, and OBSIDIAN. To prevent the BGG stellar property distributions from being biased by the X-ray properties of their IGrM, we forgo the minimum X-ray luminosity threshold used for the comparison with COSMOS in Section 4, and examine the properties of all BGGs with stellar masses $\log(M_*/M_\odot) \in [10, 12]$ that reside in groups containing at least 3 luminous galaxies. The Figure shows the sSFR – M_* plane for the full

BGG samples in the first row and for only BGGs with measurable $\log(\text{sSFR}/\text{yr}^{-1}) > -12$ in the second row. BGG populations from SIMBA, SIMBA-C, and OBSIDIAN are highlighted in the first, second, and third columns, respectively, with the formatting following that used in previous Figures. The median relations of all three simulations are shown in all columns to facilitate comparison, and each simulation's respective panel additionally contains its 16th and 84th inter-percentile shaded region and the systems beyond as data points. The black line and shaded region are the K. E. Whitaker et al. (2012) SFMS and the ± 0.75 dex region around it. The right-most panels show the simulations' sSFR distributions as normalised density histograms.

We emphasise that the point in the top row of Figure 9 where each simulation's median relation drops to $\log(\text{sSFR}/\text{yr}^{-1}) = -14$ represents the stellar mass at which $\geq 50\%$ of the BGGs in the mass bin have immeasurable sSFR. The slope of the median at this point, however, is not meaningful, as it is dependent on the arbitrary value chosen to represent immeasurable sSFRs and thus does not reflect the intrinsic slope of the sSFR– M_* relation.

The vertical pink lines that appear in every panel give an approximate stellar mass for which jet feedback may be activated in each simulation. These are estimated from the simulations' $M_{\text{BH}} - M_*$ relations from R. T. Hough et al. (2023) and D. Rennehan et al. (2024) as the stellar masses that correspond with the minimum black hole masses permitting jet feedback (see Section 2 for the specific M_{BH} values). SIMBA and SIMBA-C have two associated pink lines because jet feedback is activated within a range of SMBH masses, where the probability of activation increases with M_{BH} within the activation range, and equals 1 beyond it.

In the bottom two rows of Figure 9, we compare the simulations' BGG populations within two sSFR subsamples: BGGs with quenched sSFRs¹⁵ represented by solid lines, and those with immeasurable $\log(\text{sSFR}/\text{yr}^{-1}) \leq -12$ represented by dotted lines and hatching. In the third row, we show the fraction of each sSFR subsample contained in stellar mass bins of width 0.25 dex (N_i/N , where N_i is the number of quenched/immeasurable BGGs in bin i and N is the total number of quenched/immeasurable BGGs), and in the fourth row, the relative quenched and immeasurable fraction of all BGGs in each bin ($N_i/N_{\text{tot},i}$, where $N_{\text{tot},i}$ is the total number of BGGs in bin i). The numbers

in the lowest panels display each simulation's total fraction of BGGs with quenched (solid) and immeasurable (dotted) sSFRs.

The distinction between the proportion of BGGs with immeasurable sSFR and the proportion considered quenched is an important one. In SIMBA and its variants, immeasurable sSFR implies that no new star particles have been formed in the prior 100 Myr. An accumulation of galaxies with measurable but quenched sSFRs suggests that star formation is slowing down gradually. On the other hand, a sample containing a large fraction of immeasurable sSFRs and few that are quenched but still measurable can be indicative of a process that quenches star formation suddenly.

The latter situation can be seen in the SIMBA sample, which is dominated by BGGs with immeasurable sSFR. The onset of jet feedback in SIMBA is estimated to occur at low BGG stellar masses. Coinciding with this mass, at $\log(M_*/M_\odot) \sim 10.4$, SIMBA's median sSFR– M_* relation in the top panel of Figure 9 drops abruptly to immeasurably low sSFR. Star formation in the BGG population of SIMBA is not gradually being suppressed with increasing mass, demonstrated by $> 50\%$ of BGGs having immeasurably low sSFR for all stellar masses. This is further evidenced in the lower two panels of Figure 9, where SIMBA's relative fractions of quenched and immeasurable sSFRs stay within $\lesssim 20\%$ of one another as a function of stellar mass, and the two sSFR subsamples have nearly identical stellar mass distributions. The early onset of powerful jet feedback gives SIMBA a large proportion (54%) of BGGs with immeasurable sSFRs, contributing to a high overall quenched fraction of 72%.

This jet feedback, however, proves to be less effective at heating and removing gas from massive haloes. In the middle panel of Figure 9 SIMBA's median measurable sSFR flattens and then begins to subtly rise with stellar mass at $\log(M_*/M_\odot) \sim 10.8$, never falling below the quenched line. This can be linked to SIMBA's maximum jet velocity, which is lower than those of the other simulations and does not scale with the mass of the system. In increasingly massive systems with deeper gravitational potential wells, the AGN jet cannot sufficiently regulate star formation, leading to the excess of high-mass systems first seen in Figure 3, the dip in the median $\text{Age}_w - M_*$ relation of Figure 8, and additionally explaining the rightward shift of massive haloes in the SIMBA SMHM relation (see Figure 1 of S. L. Jung et al. 2022). In comparison to the relative quenched fractions of SIMBA-C and OBSIDIAN, BGGs in SIMBA are over quenched for $\log(M_*/M_\odot) \lesssim 11$ where the jets are efficient, and under quenched in massive systems with $\log(M_*/M_\odot) \gtrsim 11$.

¹⁵ We reiterate that BGGs are considered quenched if they fall ≥ 0.75 dex below the K. E. Whitaker et al. (2012) SFMS and as such, not all quenched sSFRs are immeasurably low.

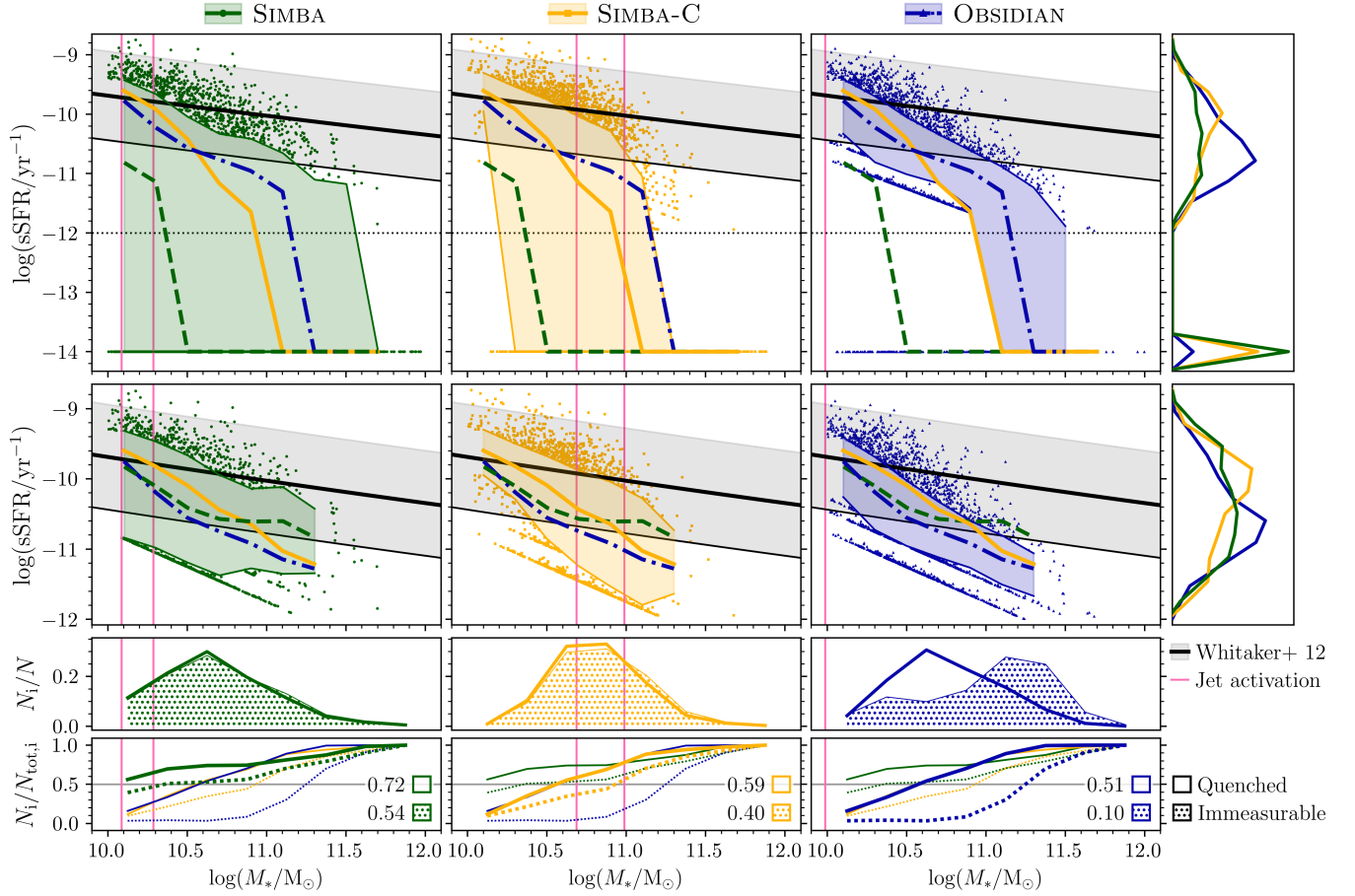


Figure 9. Overview of star formation and quenching in SIMBA and its variants for BGGs with $\log(M_*/M_\odot) \in [10, 12]$. From left to right, the first, second, and third columns respectively highlight BGGs from the SIMBA (green, dashed lines), SIMBA-C (yellow, solid lines), and OBSIDIAN (blue, dot-dashed lines) simulations. **Top row:** The sSFR – M_* relation for all sSFRs. The simulations’ median relations are shown in every panel, and each simulation’s respective column shows its 16th and 84th inter-percentile range (shaded region) and the systems beyond (data points). The black line and grey shading are the K. E. Whitaker et al. (2012) SFMS and the ± 0.75 dex region around it, below which, BGGs are considered quenched. The horizontal black dotted line is the measurable sSFR limit $\log(\text{sSFR}/\text{yr}^{-1}) = -12$. The rightmost panel in the top row contains the simulations’ sSFR distributions as density histograms. The vertical pink lines give an estimated stellar mass for which jet feedback is activated in each simulation. **Middle row:** The sSFR – M_* relation for BGGs with measurable $\log(\text{sSFR}/\text{yr}^{-1}) > -12$. The rightmost distributions are normalised with respect to the measurable sSFR sample sizes, and all other formatting follows that in the top row. **Bottom row:** A comparison between BGG subsamples with quenched (solid lines) and immeasurable $\log(\text{sSFR}/\text{yr}^{-1}) \leq -12$ (dotted lines and hatching) sSFRs. The top plot shows the fraction of each sSFR subsample contained within stellar mass bins of width 0.25 dex (N_i/N), and the bottom plot shows the relative fraction of all BGGs in the same mass bins that are immeasurable or quenched ($N_i/N_{\text{tot},i}$). The relative fractions of each simulation are on all panels for comparison, and the legends in the lowest panels show the simulations’ total fraction of BGGs in each sSFR subsample.

The ILLUSTRISTNG cosmological simulation (A. Pillepich et al. 2018a,b) implements kinetic jet feedback as randomly oriented injections of momentum that drive large-scale outflows capable of quenching galaxies (R. Weinberger et al. 2017). Like SIMBA, jets in ILLUSTRISTNG are highly efficient and tend to produce quenched fractions that are higher than observed for the majority of galaxies, while simultaneously decreasing with increasing mass (M. Donnari et al. 2021; B. D.

Oppenheimer et al. 2021; S. L. Jung et al. 2022). This further emphasises the challenge of developing and calibrating AGN feedback models that avoid both over- and under-quenching, and maintain efficient regulation in increasingly deep potential wells.

As a result of their shared two-regime AGN feedback model, SIMBA-C displays similar BGG star formation characteristics as SIMBA with distinctions tied to the recalibration of jet feedback. Like SIMBA, SIMBA-

C has nearly identical stellar mass distributions within the quenched and immeasurable sSFR subsamples (Figure 9, lower panels), lacking the significant presence of systems with measurable but quenched sSFRs. This gives SIMBA-C a large fraction of BGGs with immeasurable sSFR (40%) and a measurable sSFR distribution that peaks above the K. E. Whitaker et al. (2012) SFMS, even in the absence of any X-ray selection criteria. In contrast to SIMBA, SIMBA-C has significantly higher rates of star formation among low-mass BGGs, which contributes to a lower overall quenched fraction of 59%. This is a direct consequence of the delayed onset of jet feedback preventing low- M_* BGGs from abruptly quenching. In the top panel of Figure 9, SIMBA-C’s median sSFR drops to immeasurable at $\log(M_*/M_\odot) \sim 11$ for ~ 0.6 dex more massive systems than seen in SIMBA, but again coinciding with the estimated stellar mass at which jet feedback is initiated.

The maximum jet velocity in SIMBA-C scales with the mass of the SMBH and is capped at a significantly higher magnitude than in SIMBA, allowing the AGN feedback to maintain its effectiveness as the system grows and its gravitational potential well deepens. As such, star formation is highly suppressed in the massive systems of SIMBA-C, which can be seen in its 84th percentile sSFR dropping to immeasurable at a stellar mass only ~ 0.2 dex higher than its median. SIMBA’s inefficient jet feedback in high-mass systems causes its 84th percentile sSFR to remain in the measurable range for ~ 2.3 dex higher masses than its median. The delayed onset of jet feedback in SIMBA-C allows low- M_* BGGs to remain star-forming, but once initiated, the high-velocity jets efficiently quench star formation, preventing the continuous growth of high- M_* systems seen in SIMBA.

The AGN feedback model of OBSIDIAN has a distinctly different effect on the star formation and quenching of BGGs than the model utilised by SIMBA and SIMBA-C. Although jet feedback in OBSIDIAN is estimated to be permitted for all BGGs with $\log(M_*/M_\odot) \geq 10$, the median sSFR– M_* relation in the top panel of Figure 9 has the shallowest slope and does not drop to immeasurable sSFR until $\log(M_*/M_\odot) \sim 11.3$. Even OBSIDIAN’s 16th percentile sSFR remains quenched but measurable up to $\log(M_*/M_\odot) \sim 11$, contrasting those of SIMBA and SIMBA-C, which become immeasurable at quite low stellar masses.

Rather than experiencing an abrupt drop in sSFR as a result of jet feedback initiating, the BGG population in OBSIDIAN gradually moves off the K. E. Whitaker et al. (2012) SFMS as a function of stellar mass. In the second row of Figure 9, OBSIDIAN’s median measurable sSFR sits below those of SIMBA and SIMBA-C

for all stellar masses, despite its full sSFR– M_* relation remaining measurable up to higher masses. This highlights the contrast between the accumulation of BGGs with quenched but measurable sSFRs in OBSIDIAN, and the dichotomy of BGGs with star-forming and immeasurable sSFRs seen in SIMBA and SIMBA-C.

With total quenched and immeasurable fractions of 51% and 10% respectively, nearly all quenched BGGs in OBSIDIAN have sSFRs still in the measurable range. OBSIDIAN’s immeasurable sSFR population additionally grows with increasing stellar mass, with the fractional distribution in the third panel of Figure 9 peaking at $\log(M_*/M_\odot) > 11$; a greater mass than for the quenched subsample. As star formation is increasingly suppressed with mass, more and more massive systems become quenched to the point of forming no star particles within 100 Myr, causing the relative fractions of quenched and immeasurable sSFRs to slowly converge (Figure 9, bottom panel).

SIMBA-C and OBSIDIAN have similar rates of quenching as a function of stellar mass; however, the underlying process by which BGGs become quenched is highly degenerate. Where SIMBA-C relies on delayed jet feedback that strengthens with mass to quickly quench massive systems, OBSIDIAN incorporates constant velocity jets at all BGG stellar masses and achieves the same suppression of growth through more steady and consistent regulation. The agreement between the OBSIDIAN and COSMOS BGG populations discussed in Section 5.1 suggests that OBSIDIAN’s gradual decline in star formation is more representative of the quenching processes experienced by real massive galaxies in the universe.

Rapid quenching at a characteristic mass scale, attributed to the onset of AGN jet feedback, has traditionally been invoked as a necessary mechanism for galaxy formation models to reproduce key statistical observables, including the exponential cut-off of the GMSF, the observed galaxy colour bimodality, and the high quenched fractions of massive galaxies (R. G. Bower et al. 2006; D. J. Croton et al. 2006; C. Mancini et al. 2015; J. Lian et al. 2016; C. Hahn et al. 2017). However, both observational and theoretical studies increasingly indicate that galaxies quench over a wide range of timescales, including prolonged and gradual suppression of star formation (e.g. D. S. Tararu et al. 2014; A. Katsianis et al. 2021; S. Tacchella et al. 2022; G. Jin et al. 2025). This further suggests that the quenching pathways capable of reproducing global galaxy statistics are not unique, but rather degenerate and sensitive to the adopted feedback models and their calibration. In a recent study, G. Gawade (2025) demonstrate that central galaxies in EAGLE undergo a slow decline in star forma-

tion that matches the green valley sSFR distribution of AGN host galaxies from the Sloan Digital Sky Survey (SDSS; K. N. Abazajian et al. 2009) better than IL-LUSTRISTNG, which exhibits a rapid shutdown of star formation that largely evacuates the green valley in a similar fashion to what we see with SIMBA and SIMBA-C. Given that most cosmological simulations, including SIMBA and its variants, are calibrated to reproduce the GSMF and other global statistics, these results imply that rapid quenching may reflect the structure and tuning of specific feedback models rather than a fundamental requirement imposed by observations, and that this issue needs to be investigated further.

In the two-regime model of SIMBA and SIMBA-C, quenching is highly dependent on the activation and strength of jet feedback, with SMBHs entering jet mode if their Eddington ratio satisfies $f_{\text{Edd}} = \dot{M}_{\text{acc}}/\dot{M}_{\text{Edd}} \lesssim 0.22$. In OBSIDIAN’s three-regime model, jets are incorporated into ADAF mode, which is only entered for SMBHs with $f_{\text{Edd}} \leq 0.03$. ADAF mode requires an order of magnitude lower Eddington ratio and therefore, the SMBHs in OBSIDIAN may release jets less frequently than those under the two-regime model, relying on winds from the quasar regime ($0.03 \leq f_{\text{Edd}} \leq 0.3$) to heat and eject gas from the system.

Efficient feedback outside of ADAF mode may be a contributing factor in OBSIDIAN’s consistent regulation of star formation across all masses. AGN winds in OBSIDIAN are ejected at a constant velocity of 1000 km s^{-1} , while in the two-regime model, such velocities can only be achieved by the most massive SMBHs. S. Grayson et al. (2025) corroborate that the two-regime model’s quasar wind velocity is too low to escape deep potential wells, even with increased mass loading, and that the model relies on the high-velocity jets to quench massive galaxies.

In addition to jet feedback activating under different conditions, the two feedback models differ in the characteristics of the jets themselves. Jets in OBSIDIAN are ejected at a constant velocity of 10000 km s^{-1} (D. Rennehan et al. 2024), whereas in the two-regime model, the jet velocity scales inversely with the Eddington ratio, with values ranging from $\sim 800 \text{ km s}^{-1}$ to maxima of $\sim 8000 \text{ km s}^{-1}$ in SIMBA and 35000 km s^{-1} in SIMBA-C (R. Davé et al. 2019; R. T. Hough et al. 2023).

Additionally, all SMBH outflows in the two-regime model are ejected in a bipolar fashion, parallel to the direction of the angular momentum vector of the accreting gas, with the jets changing direction on timescales of $0.3 - 0.5 \text{ Gyr}$ (Fred Jennings, private communication). While the AGN winds in OBSIDIAN are similarly aligned or anti-aligned with the local angular momen-

tum, ADAF jets are ejected in a randomly selected direction over 4π steradians. Evidence of misalignment between the rotation axes of the accretion disc (the jet axis) and the galaxy disc has been found in both observational studies (J. F. Gallimore et al. 2006; P. Pjanka et al. 2017) and high-resolution cosmological zoom simulations (D. Anglés-Alcázar et al. 2021; P. F. Hopkins et al. 2024). Reorienting jets have been shown to have a higher coupling with the IGrM (S. Cielo et al. 2018), possibly explaining why OBSIDIAN jets are able to suppress cooling flows from fuelling BGG star formation without requiring as high ejection velocities as in SIMBA-C. We refer readers to K.-Y. Su et al. (2021) for a comprehensive analysis of how the efficiency of various jet feedback models depends on a wide range of parameters, including jet velocity and precession angle.

OBSIDIAN is one of the first of a new generation of cosmological simulations characterised by the development of increasingly sophisticated and physically motivated AGN feedback models. Another recent example, which also incorporates three feedback regimes partitioned by the Eddington ratio, is the F. Huško et al. (2025) model implemented in the COLIBRE simulation suite (E. Chaikin et al. 2025a; J. Schaye et al. 2025). Across all regimes, this prescription employs both kinetic jet feedback and the C. M. Booth & J. Schaye (2009) thermal feedback mechanism (see Section 5.2.1). E. Chaikin et al. (2025b) show that COLIBRE broadly reproduces observed quenched fractions over a wide redshift range, although it exhibits signs of reduced quenching in the most massive systems at $z < 2$, including central galaxies (see Figures 9 and 10 of E. Chaikin et al. 2025b).

Uncovering in detail how the OBSIDIAN model effectively regulates the growth of massive galaxies through gradual suppression of star formation requires a thorough investigation into how SMBHs in OBSIDIAN evolve over cosmic time. While such an analysis is beyond the scope of this paper, future work will focus on in-depth case studies of individual SMBHs in SIMBA, SIMBA-C, and OBSIDIAN. This will involve tracking the growth of SMBHs and how they transition between regimes of feedback, as well as examining properties of the resulting outflows and how they shape the galaxies they inhabit.

6. CONCLUSIONS

In this work, we investigate the stellar properties of BGGs in four cosmological simulations: ROMULUS, SIMBA, SIMBA-C, and OBSIDIAN, and compare the simulated results with observed BGGs from the COSMOS field. We find that the properties of BGG populations in simulations are strongly impacted by the strength

and mechanism of their respective AGN feedback model. Our most significant results are summarised as follows:

- BGG stellar properties from the OBSIDIAN simulation align best with COSMOS observations. Two-sample KS tests find compatibility between the OBSIDIAN and COSMOS distributions of stellar mass, measurable sSFR when split into low- and high- M_* subsamples, and stellar age for low- M_* BGGs. OBSIDIAN and COSMOS show the highest agreement in their total BGG quenched fractions of 88% and 91% respectively, as well as in their relative quenched fractions as a function of stellar mass. The OBSIDIAN and COSMOS samples are in good agreement on the sSFR– M_* plane, with the bulk of their BGGs that have measurable sSFR ($\log(\text{sSFR}/\text{yr}^{-1}) > -12$) falling below the K. E. Whitaker et al. (2012) SFMS.

- BGGs in the ROMULUS simulations have significantly higher rates of star formation compared to the other simulations and COSMOS observations. ROMULUS25 has a low quenched fraction of 22%, with the majority of BGGs closely following the K. E. Whitaker et al. (2012) SFMS without strong evidence of increased quenching in massive systems. This is a result of ROMULUS' thermal AGN feedback model being inefficient at heating and expelling gas from haloes so as to prevent cooling flows from fuelling BGG star formation.

- In SIMBA, the onset of AGN Jet feedback occurs at low stellar masses, causing $> 50\%$ of SIMBA BGGs to have immeasurably low sSFRs for $\log(M_*/M_\odot) \gtrsim 10.4$. SIMBA's maximum jet ejection velocity is low and does not scale with the mass of the system, resulting in jet feedback becoming less efficient at regulating the growth of massive systems with deep gravitational potential wells. This leads to SIMBA exhibiting a rise in sSFR for $\log(M_*/M_\odot) \gtrsim 10.8$ and an excess of massive BGGs. The presence of massive BGGs with young stellar populations gives SIMBA the highest agreement with COSMOS for BGG mass-weighted stellar age.

- SIMBA-C has delayed onset jet feedback, which results in low- M_* BGGs having increased star formation and higher masses of hot gas compared to SIMBA. The significant presence of low- M_* , star-forming BGGs drives disagreement between SIMBA-C and COSMOS for all BGG stellar properties. SIMBA-C's maximum jet ejection velocity scales with the mass of the system and can reach much higher magnitudes than in SIMBA. Because of this, following the activation of jet feedback for $\log(M_*/M_\odot) \gtrsim 11$, SIMBA-C BGGs swiftly fall off the K. E. Whitaker et al. (2012) SFMS and their sSFRs become immeasurably low.

- The two-regime kinetic AGN feedback model of SIMBA and SIMBA-C heavily relies on the strength and

onset mass of jet feedback to quench BGGs. At the point where jet feedback is initiated, the majority of BGGs are quenched abruptly as a function of mass, which results in the bulk of the BGG populations existing in a dichotomy between those following the SFMS and those that have immeasurably low sSFRs. The three-regime OBSIDIAN feedback model promotes quenching through a gradual decline in star formation as a function of stellar mass, which manifests in an accumulation of BGGs that are quenched, but have sSFRs still in the measurable range. The agreement seen in the sSFR– M_* plane of OBSIDIAN and COSMOS implies that this gradual quenching process is reminiscent of that experienced by real BGGs.

Group environments and their central BGGs are important test beds for investigating how galaxy formation models reproduce the physical processes taking place in massive, dynamic systems. Our results reinforce that the modelling of AGN feedback is critical for regulating the growth of massive galaxies, driving their global properties and underlying evolutionary pathways. Future work will involve a detailed investigation into the joint evolution of galaxies and their SMBH that allows the AGN feedback model of OBSIDIAN to achieve steady regulation of star formation in BGGs across all stellar masses. OBSIDIAN's success in the group regime demonstrates the value of physically motivated subgrid prescriptions in capturing the complex processes, like SMBH feedback, shaping massive galaxies.

ACKNOWLEDGMENTS

The simulation analysis reported in this article was enabled by HPC resources provided by the Digital Research Alliance of Canada (<https://www.alliancecan.ca/en>) awarded to AB, specifically SciNet's Niagara and Trillium computing clusters. The SIMBA-C and OBSIDIAN simulations were simulated and accessed on the Flatiron Institute's research computing facilities (the Iron compute cluster), supported by the Simons Foundation. Computational resources for ROMULUS were part of a PRAC allocation supported by the National Science Foundation (award number OAC-1613674). Other resources for ROMULUS were provided by ACCESS (formerly XSEDE) resources at SDSC and TACC. ACCESS is supported by National Science Foundation grants 2138259, 2138286, 2138307, 2137603, and 2138296. RB acknowledges the SIMBA collaboration for the use of their simulations and the COSMOS collaboration for allowing access to their catalogues. RB also acknowledges Guruvayurappan Balaji for providing ROMULUS data files necessary for tracking galaxies over time.

AB acknowledges the support of the Natural Sciences and Engineering Research Council of Canada (NSERC) through its Discovery Grant program. AB also acknowledges support from the Infosys Foundation via an endowed Infosys Visiting Chair Professorship at the Indian Institute of Science and from the Leverhulme Trust via the Leverhulme Visiting Professorship at the University of Edinburgh. AB would like to thank the Dept. of Physics (IISc) and IfA (Univ. of Edinburgh) for hospitality during his recent visits. Finally, we acknowledge and respect the Lek'wəŋən (Songhees and Xwəsepəm̓/Esquimalt) Peoples on whose traditional territory the University of Victoria stands, and the Lek'wəŋən and WSÁNEĆ Peoples whose historical relationships with the land continue to this day.

AUTHOR CONTRIBUTIONS

RB performed the analysis and wrote the manuscript, with guidance from AB, DR, and RD. GG and AF provided the COSMOS group catalogue and contributed to the discussion of sample selection techniques. All other co-authors contributed to developing analysis techniques and providing insights about the detailed nature of feedback in the ROMULUS, SIMBA, SIMBA-C, and OBSIDIAN simulations, as well as engaged in discussions that helped sharpen this paper.

REFERENCES

Abazajian, K. N., Adelman-McCarthy, J. K., Agüeros, M. A., et al. 2009, *ApJS*, 182, 543, doi: [10.1088/0067-0049/182/2/543](https://doi.org/10.1088/0067-0049/182/2/543)

Ade, P. a. R., Aghanim, N., Arnaud, M., et al. 2016, *A&A*, 594, A13, doi: [10.1051/0004-6361/201525830](https://doi.org/10.1051/0004-6361/201525830)

Aghanim, N., Akrami, Y., Ashdown, M., et al. 2020, *A&A*, 641, A6, doi: [10.1051/0004-6361/201833910](https://doi.org/10.1051/0004-6361/201833910)

Anglés-Alcázar, D., Davé, R., Faucher-Giguère, C.-A., Özel, F., & Hopkins, P. F. 2017a, *MNRAS*, 464, 2840, doi: [10.1093/mnras/stw2565](https://doi.org/10.1093/mnras/stw2565)

Anglés-Alcázar, D., Faucher-Giguère, C.-A., Quataert, E., et al. 2017b, *MNRAS: Letters*, 472, L109, doi: [10.1093/mnrasl/slx161](https://doi.org/10.1093/mnrasl/slx161)

Anglés-Alcázar, D., Quataert, E., Hopkins, P. F., et al. 2021, *ApJ*, 917, 53, doi: [10.3847/1538-4357/ac09e8](https://doi.org/10.3847/1538-4357/ac09e8)

Appleby, S., Davé, R., Sorini, D., Cui, W., & Christiansen, J. 2023, *MNRAS*, 519, 5514, doi: [10.1093/mnras/stad025](https://doi.org/10.1093/mnras/stad025)

Arnouts, S., Moscardini, L., Vanzella, E., et al. 2002, *MNRAS*, 329, 355, doi: [10.1046/j.1365-8711.2002.04988.x](https://doi.org/10.1046/j.1365-8711.2002.04988.x)

Babul, A. 1991, *MNRAS*, 248, 177, doi: [10.1093/mnras/248.2.177](https://doi.org/10.1093/mnras/248.2.177)

Babul, A., Balogh, M. L., Lewis, G. F., & Poole, G. B. 2002, *MNRAS*, 330, 329, doi: [10.1046/j.1365-8711.2002.05044.x](https://doi.org/10.1046/j.1365-8711.2002.05044.x)

Benson, A. J., & Babul, A. 2009, *MNRAS*, 397, 1302, doi: [10.1111/j.1365-2966.2009.15087.x](https://doi.org/10.1111/j.1365-2966.2009.15087.x)

Bianconi, M., Smith, G. P., Haines, C. P., et al. 2018, *MNRAS: Letters*, 473, L79, doi: [10.1093/mnrasl/slx167](https://doi.org/10.1093/mnrasl/slx167)

Bildfell, C., Hoekstra, H., Babul, A., & Mahdavi, A. 2008, *MNRAS*, 389, 1637, doi: [10.1111/j.1365-2966.2008.13699.x](https://doi.org/10.1111/j.1365-2966.2008.13699.x)

Bondi, H. 1952, *MNRAS*, 112, 195, doi: [10.1093/mnras/112.2.195](https://doi.org/10.1093/mnras/112.2.195)

Booth, C. M., & Schaye, J. 2009, *MNRAS*, 398, 53, doi: [10.1111/j.1365-2966.2009.15043.x](https://doi.org/10.1111/j.1365-2966.2009.15043.x)

Bothwell, M. S., Kenicutt, R. C., Johnson, B. D., et al. 2011, *MNRAS*, 415, 1815, doi: [10.1111/j.1365-2966.2011.18829.x](https://doi.org/10.1111/j.1365-2966.2011.18829.x)

Bower, R. G., Benson, A. J., Malbon, R., et al. 2006, *MNRAS*, 370, 645, doi: [10.1111/j.1365-2966.2006.10519.x](https://doi.org/10.1111/j.1365-2966.2006.10519.x)

Bruzual, G., & Charlot, S. 2003, *MNRAS*, 344, 1000, doi: [10.1046/j.1365-8711.2003.06897.x](https://doi.org/10.1046/j.1365-8711.2003.06897.x)

Caleb, M., Flynn, C., & Stappers, B. W. 2019, *MNRAS*, 485, 2281, doi: [10.1093/mnras/stz571](https://doi.org/10.1093/mnras/stz571)

Calzetti, D. 2013, in *Secular Evolution of Galaxies* (Cambridge University Press), 419–458, doi: [10.1017/CBO9781139547420.008](https://doi.org/10.1017/CBO9781139547420.008)

Chabrier, G. 2003, *PASP*, 115, 763, doi: [10.1086/376392](https://doi.org/10.1086/376392)

Chaikin, E., Schaye, J., Schaller, M., et al. 2025a, *arXiv*, doi: [10.48550/arXiv.2509.04067](https://doi.org/10.48550/arXiv.2509.04067)

Chaikin, E., Schaye, J., Schaller, M., et al. 2025b, *arXiv*, doi: [10.48550/arXiv.2509.07960](https://doi.org/10.48550/arXiv.2509.07960)

Choi, E., Ostriker, J. P., Naab, T., & Johansson, P. H. 2012, *ApJ*, 754, 125, doi: [10.1088/0004-637X/754/2/125](https://doi.org/10.1088/0004-637X/754/2/125)

Christensen, C. R., Governato, F., Quinn, T., et al. 2014, *MNRAS*, 440, 2843, doi: [10.1093/mnras/stu399](https://doi.org/10.1093/mnras/stu399)

Cielo, S., Babul, A., Antonuccio-Delogu, V., Silk, J., & Volonteri, M. 2018, *A&A*, 617, A58, doi: [10.1051/0004-6361/201832582](https://doi.org/10.1051/0004-6361/201832582)

Conroy, C. 2013, *ARA&A*, 51, 393, doi: [10.1146/annurev-astro-082812-141017](https://doi.org/10.1146/annurev-astro-082812-141017)

Cougo, J., Rembold, S. B., Ferrari, F., & Kaipper, A. L. P. 2020, *MNRAS*, 498, 4433, doi: [10.1093/mnras/staa2688](https://doi.org/10.1093/mnras/staa2688)

Cowles, M., & Davis, C. 1982, *American Psychologist*, 37, 553, doi: [10.1037/0003-066X.37.5.553](https://doi.org/10.1037/0003-066X.37.5.553)

Crain, R. A., & van de Voort, F. 2023, *ARA&A*, 61, 473, doi: [10.1146/annurev-astro-041923-043618](https://doi.org/10.1146/annurev-astro-041923-043618)

Crain, R. A., Schaye, J., Bower, R. G., et al. 2015, *MNRAS*, 450, 1937, doi: [10.1093/mnras/stv725](https://doi.org/10.1093/mnras/stv725)

Croton, D. J. 2013, *PASA*, 30, e052, doi: [10.1017/pasa.2013.31](https://doi.org/10.1017/pasa.2013.31)

Croton, D. J., Springel, V., White, S. D. M., et al. 2006, *MNRAS*, 365, 11, doi: [10.1111/j.1365-2966.2005.09675.x](https://doi.org/10.1111/j.1365-2966.2005.09675.x)

Davé, R., Anglés-Alcázar, D., Narayanan, D., et al. 2019, *MNRAS*, 486, 2827, doi: [10.1093/mnras/stz937](https://doi.org/10.1093/mnras/stz937)

Davé, R., Crain, R. A., Stevens, A. R. H., et al. 2020, *MNRAS*, 497, 146, doi: [10.1093/mnras/staa1894](https://doi.org/10.1093/mnras/staa1894)

Davé, R., Thompson, R., & Hopkins, P. F. 2016, *MNRAS*, 462, 3265, doi: [10.1093/mnras/stw1862](https://doi.org/10.1093/mnras/stw1862)

Donnari, M., Pillepich, A., Nelson, D., et al. 2021, *MNRAS*, 506, 4760, doi: [10.1093/mnras/stab1950](https://doi.org/10.1093/mnras/stab1950)

Donnari, M., Pillepich, A., Nelson, D., et al. 2019, *MNRAS*, 485, 4817, doi: [10.1093/mnras/stz712](https://doi.org/10.1093/mnras/stz712)

Dubois, Y., Devriendt, J., Teyssier, R., & Slyz, A. 2011, *MNRAS*, 417, 1853, doi: [10.1111/j.1365-2966.2011.19381.x](https://doi.org/10.1111/j.1365-2966.2011.19381.x)

Edwards, L. O. V., Salinas, M., Stanley, S., et al. 2020, *MNRAS*, 491, 2617, doi: [10.1093/mnras/stz2706](https://doi.org/10.1093/mnras/stz2706)

Einasto, M., Einasto, J., Tenjes, P., et al. 2024, *A&A*, 681, A91, doi: [10.1051/0004-6361/202347504](https://doi.org/10.1051/0004-6361/202347504)

Figueira, M., Pollo, A., Małek, K., et al. 2022, *A&A*, 667, A29, doi: [10.1051/0004-6361/202141701](https://doi.org/10.1051/0004-6361/202141701)

Finoguenov, A., Guzzo, L., Hasinger, G., et al. 2007, *ApJS*, 172, 182, doi: [10.1086/516577](https://doi.org/10.1086/516577)

Finoguenov, A., Connelly, J. L., Parker, L. C., et al. 2009, *ApJ*, 704, 564, doi: [10.1088/0004-637X/704/1/564](https://doi.org/10.1088/0004-637X/704/1/564)

Finoguenov, A., Watson, M. G., Tanaka, M., et al. 2010, *MNRAS*, 403, 2063, doi: [10.1111/j.1365-2966.2010.16256.x](https://doi.org/10.1111/j.1365-2966.2010.16256.x)

Finoguenov, A., Tanaka, M., Cooper, M., et al. 2015, *A&A*, 576, A130, doi: [10.1051/0004-6361/201323053](https://doi.org/10.1051/0004-6361/201323053)

Flores Velázquez, J. A., Gurvich, A. B., Faucher-Giguère, C.-A., et al. 2021, *MNRAS*, 501, 4812, doi: [10.1093/mnras/staa3893](https://doi.org/10.1093/mnras/staa3893)

Foster, A., Smith, R. K., Brickhouse, N. S., & Cui, X. 2016, in *AAS/High Energy Astrophysics Division #15*, Vol. 15, 116.18

Foster, A. R., & Heuer, K. 2020, *Atoms*, 8, 49, doi: [10.3390/atoms8030049](https://doi.org/10.3390/atoms8030049)

Foster, A. R., Heuer, K., & Smith, R. 2021, *Bull. AAS*, 53

Fukugita, M., & Kawasaki, M. 2003, *MNRAS*, 340, L7, doi: [10.1046/j.1365-8711.2003.06507.x](https://doi.org/10.1046/j.1365-8711.2003.06507.x)

Furnell, K. E., Collins, C. A., Kelvin, L. S., et al. 2018, *MNRAS*, 478, 4952, doi: [10.1093/mnras/sty991](https://doi.org/10.1093/mnras/sty991)

Gallazzi, A., Bell, E. F., Zibetti, S., Brinchmann, J., & Kelson, D. D. 2014, *ApJ*, 788, 72, doi: [10.1088/0004-637X/788/1/72](https://doi.org/10.1088/0004-637X/788/1/72)

Gallimore, J. F., Axon, D. J., O'Dea, C. P., Baum, S. A., & Pedlar, A. 2006, *AJ*, 132, 546, doi: [10.1086/504593](https://doi.org/10.1086/504593)

Gawade, G. 2025, *arXiv*, doi: [10.48550/arXiv.2512.22268](https://doi.org/10.48550/arXiv.2512.22268)

George, M. R., Leauthaud, A., Bundy, K., et al. 2011, *ApJ*, 742, 125, doi: [10.1088/0004-637X/742/2/125](https://doi.org/10.1088/0004-637X/742/2/125)

Gozaliasl, G., Finoguenov, A., Khosroshahi, H. G., et al. 2016, *MNRAS*, 458, 2762, doi: [10.1093/mnras/stw448](https://doi.org/10.1093/mnras/stw448)

Gozaliasl, G., Finoguenov, A., Khosroshahi, H. G., et al. 2014, *A&A*, 566, A140, doi: [10.1051/0004-6361/201322459](https://doi.org/10.1051/0004-6361/201322459)

Gozaliasl, G., Finoguenov, A., Khosroshahi, H. G., et al. 2018, *MNRAS*, 475, 2787, doi: [10.1093/mnras/sty003](https://doi.org/10.1093/mnras/sty003)

Gozaliasl, G., Finoguenov, A., Tanaka, M., et al. 2019, *MNRAS*, 483, 3545, doi: [10.1093/mnras/sty3203](https://doi.org/10.1093/mnras/sty3203)

Gozaliasl, G., Finoguenov, A., Khosroshahi, H. G., et al. 2020, *A&A*, 635, A36, doi: [10.1051/0004-6361/201936745](https://doi.org/10.1051/0004-6361/201936745)

Gozaliasl, G., Finoguenov, A., Babul, A., et al. 2024, *A&A*, 690, A315, doi: [10.1051/0004-6361/202449543](https://doi.org/10.1051/0004-6361/202449543)

Gozaliasl, G., Yang, L., Kartaltepe, S. J., et al. 2025, *A&A*, doi: [10.1051/0004-6361/202556085](https://doi.org/10.1051/0004-6361/202556085)

Grayson, S., Scannapieco, E., Davé, R., Babul, A., & Hough, R. T. 2025, *arXiv*, doi: [10.48550/arXiv.2510.19924](https://doi.org/10.48550/arXiv.2510.19924)

Habouzit, M., Volonteri, M., & Dubois, Y. 2017, *MNRAS*, 468, 3935, doi: [10.1093/mnras/stx666](https://doi.org/10.1093/mnras/stx666)

Hafen, Z., Faucher-Giguère, C.-A., Anglés-Alcázar, D., et al. 2019, *MNRAS*, 488, 1248, doi: [10.1093/mnras/stz1773](https://doi.org/10.1093/mnras/stz1773)

Hahn, C., Tinker, J. L., & Wetzel, A. 2017, *ApJ*, 841, 6, doi: [10.3847/1538-4357/aa6d6b](https://doi.org/10.3847/1538-4357/aa6d6b)

Henden, N. A., Puchwein, E., Shen, S., & Sijacki, D. 2018, *MNRAS*, 479, 5385, doi: [10.1093/mnras/sty1780](https://doi.org/10.1093/mnras/sty1780)

Henden, N. A., Puchwein, E., & Sijacki, D. 2020, *MNRAS*, 498, 2114, doi: [10.1093/mnras/staa2235](https://doi.org/10.1093/mnras/staa2235)

Hopkins, P. F. 2015, *MNRAS*, 450, 53, doi: [10.1093/mnras/stv195](https://doi.org/10.1093/mnras/stv195)

Hopkins, P. F. 2017, *arXiv*, doi: [10.48550/arXiv.1712.01294](https://doi.org/10.48550/arXiv.1712.01294)

Hopkins, P. F., & Quataert, E. 2011, *MNRAS*, 415, 1027, doi: [10.1111/j.1365-2966.2011.18542.x](https://doi.org/10.1111/j.1365-2966.2011.18542.x)

Hopkins, P. F., Wellons, S., Anglés-Alcázar, D., Faucher-Giguère, C.-A., & Grudić, M. Y. 2022, *MNRAS*, 510, 630, doi: [10.1093/mnras/stab3458](https://doi.org/10.1093/mnras/stab3458)

Hopkins, P. F., Grudic, M. Y., Su, K.-Y., et al. 2024, *OJAp*, 7, doi: [10.48550/arXiv.2309.13115](https://doi.org/10.48550/arXiv.2309.13115)

Hough, R. T., Rennehan, D., Kobayashi, C., et al. 2023, *MNRAS*, 525, 1061, doi: [10.1093/mnras/stad2394](https://doi.org/10.1093/mnras/stad2394)

Hough, R. T., Shao, Z., Cui, W., et al. 2024, *MNRAS*, 532, 476, doi: [10.1093/mnras/stae1435](https://doi.org/10.1093/mnras/stae1435)

Hunt, L. K., Looze, I. D., Boquien, M., et al. 2019, *A&A*, 621, A51, doi: [10.1051/0004-6361/201834212](https://doi.org/10.1051/0004-6361/201834212)

Huško, F., Lacey, C. G., Schaye, J., et al. 2025, arXiv, doi: [10.48550/arXiv.2509.05179](https://doi.org/10.48550/arXiv.2509.05179)

Ilbert, O., Arnouts, S., McCracken, H. J., et al. 2006, *A&A*, 457, 841, doi: [10.1051/0004-6361:20065138](https://doi.org/10.1051/0004-6361:20065138)

Ilbert, O., Arnouts, S., Le Floc'h, E., et al. 2015, *A&A*, 579, A2, doi: [10.1051/0004-6361/201425176](https://doi.org/10.1051/0004-6361/201425176)

Iyer, K. G., Tacchella, S., Genel, S., et al. 2020, *MNRAS*, 498, 430, doi: [10.1093/mnras/staa2150](https://doi.org/10.1093/mnras/staa2150)

Jackson, T. M., Pasquali, A., Pacifici, C., et al. 2020, *MNRAS*, 497, 4262, doi: [10.1093/mnras/staa2306](https://doi.org/10.1093/mnras/staa2306)

Jennings, F., & Davé, R. 2023, *MNRAS*, 526, 1367, doi: [10.1093/mnras/stad2666](https://doi.org/10.1093/mnras/stad2666)

Jin, G., Kauffmann, G., Dai, Y. S., Hardcastle, M. J., & Yue, B. 2025, arXiv, doi: [10.48550/arXiv.2512.11694](https://doi.org/10.48550/arXiv.2512.11694)

Jung, S. L., Rennehan, D., Saeedzadeh, V., et al. 2022, *MNRAS*, 515, 22, doi: [10.1093/mnras/stac1622](https://doi.org/10.1093/mnras/stac1622)

Katsianis, A., Xu, H., Yang, X., et al. 2021, *MNRAS*, 500, 2036, doi: [10.1093/mnras/staa3236](https://doi.org/10.1093/mnras/staa3236)

Kennicutt, R. 1998, *ApJ*, 498, 541, doi: [10.1086/305588](https://doi.org/10.1086/305588)

Knebe, A., Knollmann, S. R., Muldrew, S. I., et al. 2011, *MNRAS*, 415, 2293, doi: [10.1111/j.1365-2966.2011.18858.x](https://doi.org/10.1111/j.1365-2966.2011.18858.x)

Knollmann, S. R., & Knebe, A. 2009, *ApJS*, 182, 608, doi: [10.1088/0067-0049/182/2/608](https://doi.org/10.1088/0067-0049/182/2/608)

Kobayashi, C., Karakas, A. I., & Lugaro, M. 2020a, *ApJ*, 900, 179, doi: [10.3847/1538-4357/abae65](https://doi.org/10.3847/1538-4357/abae65)

Kobayashi, C., Leung, S.-C., & Nomoto, K. 2020b, *ApJ*, 895, 138, doi: [10.3847/1538-4357/ab8e44](https://doi.org/10.3847/1538-4357/ab8e44)

Kolokythas, K., O'Sullivan, E., Intema, H., et al. 2019, *MNRAS*, 489, 2488, doi: [10.1093/mnras/stz2082](https://doi.org/10.1093/mnras/stz2082)

Kolokythas, K., O'Sullivan, E., Raychaudhury, S., et al. 2018, *MNRAS*, 481, 1550, doi: [10.1093/mnras/sty2030](https://doi.org/10.1093/mnras/sty2030)

Kolokythas, K., Vaddi, S., O'Sullivan, E., et al. 2022, *MNRAS*, 510, 4191, doi: [10.1093/mnras/stab3699](https://doi.org/10.1093/mnras/stab3699)

Koudmani, S., Somerville, R. S., Sijacki, D., et al. 2024, *MNRAS*, 532, 60, doi: [10.1093/mnras/stae1422](https://doi.org/10.1093/mnras/stae1422)

Kravtsov, A. V., Vikhlinin, A. A., & Meshcheryakov, A. V. 2018, *Astron. Lett.*, 44, 8, doi: [10.1134/S1063773717120015](https://doi.org/10.1134/S1063773717120015)

Kroupa, P. 2001, *MNRAS*, 322, 231, doi: [10.1046/j.1365-8711.2001.04022.x](https://doi.org/10.1046/j.1365-8711.2001.04022.x)

Krumholz, M. R., & Gnedin, N. Y. 2011, *ApJ*, 729, 36, doi: [10.1088/0004-637X/729/1/36](https://doi.org/10.1088/0004-637X/729/1/36)

Kugel, R., Schaye, J., Schaller, M., et al. 2023, *MNRAS*, 526, 6103, doi: [10.1093/mnras/stad2540](https://doi.org/10.1093/mnras/stad2540)

Kuutma, T., Poudel, A., Einasto, M., et al. 2020, *A&A*, 639, A71, doi: [10.1051/0004-6361/201937282](https://doi.org/10.1051/0004-6361/201937282)

Laigle, C., McCracken, H. J., Ilbert, O., et al. 2016, *ApJS*, 224, 24, doi: [10.3847/0067-0049/224/2/24](https://doi.org/10.3847/0067-0049/224/2/24)

Li, S.-S., Hoekstra, H., Kuijken, K., Schaller, M., & Schaye, J. 2025, *A&A*, 700, A202, doi: [10.1051/0004-6361/202452892](https://doi.org/10.1051/0004-6361/202452892)

Lian, J., Yan, R., Zhang, K., & Kong, X. 2016, *ApJ*, 832, 29, doi: [10.3847/0004-637X/832/1/29](https://doi.org/10.3847/0004-637X/832/1/29)

Liang, L., Durier, F., Babul, A., et al. 2016, *MNRAS*, 456, 4266, doi: [10.1093/mnras/stv2840](https://doi.org/10.1093/mnras/stv2840)

Liu, F. S., Xia, X. Y., Mao, S., Wu, H., & Deng, Z. G. 2008, *MNRAS*, 385, 23, doi: [10.1111/j.1365-2966.2007.12818.x](https://doi.org/10.1111/j.1365-2966.2007.12818.x)

Loubser, S. I. 2019, *Proceedings of the IAU*, 14, 255, doi: [10.1017/S1743921319008123](https://doi.org/10.1017/S1743921319008123)

Loubser, S. I., Babul, A., Hoekstra, H., et al. 2016, *MNRAS*, 456, 1565, doi: [10.1093/mnras/stv2784](https://doi.org/10.1093/mnras/stv2784)

Loubser, S. I., Hoekstra, H., Babul, A., & O'Sullivan, E. 2018, *MNRAS*, 477, 335, doi: [10.1093/mnras/sty498](https://doi.org/10.1093/mnras/sty498)

Loubser, S. I., Lagos, P., Babul, A., et al. 2022, *MNRAS*, 515, 1104, doi: [10.1093/mnras/stac1781](https://doi.org/10.1093/mnras/stac1781)

Luparello, H. E., Lares, M., Paz, D., et al. 2015, *MNRAS*, 448, 1483, doi: [10.1093/mnras/stv082](https://doi.org/10.1093/mnras/stv082)

Lupi, A., Haardt, F., Dotti, M., et al. 2016, *MNRAS*, 456, 2993, doi: [10.1093/mnras/stv2877](https://doi.org/10.1093/mnras/stv2877)

Mancini, C., Renzini, A., Daddi, E., et al. 2015, *MNRAS*, 450, 763, doi: [10.1093/mnras/stv608](https://doi.org/10.1093/mnras/stv608)

Marini, I., Borgani, S., Saro, A., et al. 2021, *MNRAS*, 507, 5780, doi: [10.1093/mnras/stab2518](https://doi.org/10.1093/mnras/stab2518)

Martínez, H. J., Coenda, V., & Muriel, H. 2013, *A&A*, 557, A61, doi: [10.1051/0004-6361/201321931](https://doi.org/10.1051/0004-6361/201321931)

Martizzi, D., Jimmy, Teyssier, R., & Moore, B. 2014, *MNRAS*, 443, 1500, doi: [10.1093/mnras/stu1233](https://doi.org/10.1093/mnras/stu1233)

McCarthy, I. G., Schaye, J., Bird, S., & Le Brun, A. M. C. 2017, *MNRAS*, 465, 2936, doi: [10.1093/mnras/stw2792](https://doi.org/10.1093/mnras/stw2792)

Menon, H., Wesolowski, L., Zheng, G., et al. 2015, *Comput. Astrophys.*, 2, 1, doi: [10.1186/s40668-015-0007-9](https://doi.org/10.1186/s40668-015-0007-9)

Ni, Y., Genel, S., Anglés-Alcázar, D., et al. 2023, *ApJ*, 959, 136, doi: [10.3847/1538-4357/ad022a](https://doi.org/10.3847/1538-4357/ad022a)

Nipoti, C. 2017, *MNRAS*, 467, 661, doi: [10.1093/mnras/stx112](https://doi.org/10.1093/mnras/stx112)

Olivares, V., Salomé, P., Hamer, S. L., et al. 2022, *A&A*, 666, A94, doi: [10.1051/0004-6361/202142475](https://doi.org/10.1051/0004-6361/202142475)

Oppenheimer, B. D., Babul, A., Bahé, Y., Butsky, I. S., & McCarthy, I. G. 2021, *Universe*, 7, 209, doi: [10.3390/universe7070209](https://doi.org/10.3390/universe7070209)

O'Sullivan, E., Ponman, T. J., Kolokythas, K., et al. 2017, *MNRAS*, 472, 1482, doi: [10.1093/mnras/stx2078](https://doi.org/10.1093/mnras/stx2078)

Padawer-Blatt, A., Shao, Z., Hough, R. T., et al. 2025, *Universe*, 11, 47, doi: [10.3390/universe11020047](https://doi.org/10.3390/universe11020047)

Peeples, M. S., Corlies, L., Tumlinson, J., et al. 2019, *ApJ*, 873, 129, doi: [10.3847/1538-4357/ab0654](https://doi.org/10.3847/1538-4357/ab0654)

Pillepich, A., Nelson, D., Hernquist, L., et al. 2018a, MNRAS, 475, 648, doi: [10.1093/mnras/stx3112](https://doi.org/10.1093/mnras/stx3112)

Pillepich, A., Springel, V., Nelson, D., et al. 2018b, MNRAS, 473, 4077, doi: [10.1093/mnras/stx2656](https://doi.org/10.1093/mnras/stx2656)

Pjanka, P., Greene, J. E., Seth, A. C., et al. 2017, ApJ, 844, 165, doi: [10.3847/1538-4357/aa7c18](https://doi.org/10.3847/1538-4357/aa7c18)

Pokhrel, R., Gutermuth, R. A., Krumholz, M. R., et al. 2021, ApJL, 912, L19, doi: [10.3847/2041-8213/abf564](https://doi.org/10.3847/2041-8213/abf564)

Pontzen, A., & Tremmel, M. 2018, ApJS, 237, 23, doi: [10.3847/1538-4365/aac832](https://doi.org/10.3847/1538-4365/aac832)

Power, C., Navarro, J. F., Jenkins, A., et al. 2003, MNRAS, 338, 14, doi: [10.1046/j.1365-8711.2003.05925.x](https://doi.org/10.1046/j.1365-8711.2003.05925.x)

Ragone-Figueroa, C., Granato, G. L., Borgani, S., et al. 2020, MNRAS, 495, 2436, doi: [10.1093/mnras/staa1389](https://doi.org/10.1093/mnras/staa1389)

Ragone-Figueroa, C., Granato, G. L., Ferraro, M. E., et al. 2018, MNRAS, 479, 1125, doi: [10.1093/mnras/sty1639](https://doi.org/10.1093/mnras/sty1639)

Ragone-Figueroa, C., Granato, G. L., Murante, G., Borgani, S., & Cui, W. 2013, MNRAS, 436, 1750, doi: [10.1093/mnras/stt1693](https://doi.org/10.1093/mnras/stt1693)

Rennehan, D. 2024, ApJ, 975, 114, doi: [10.3847/1538-4357/ad793d](https://doi.org/10.3847/1538-4357/ad793d)

Rennehan, D., Babul, A., Hayward, C. C., et al. 2020, MNRAS, 493, 4607, doi: [10.1093/mnras/staa541](https://doi.org/10.1093/mnras/staa541)

Rennehan, D., Babul, A., Moa, B., & Davé, R. 2024, MNRAS, 532, 4793, doi: [10.1093/mnras/stae1785](https://doi.org/10.1093/mnras/stae1785)

Saeedzadeh, V., Babul, A., Mukherjee, S., et al. 2024a, ApJ, 975, 265, doi: [10.3847/1538-4357/ad7a6f](https://doi.org/10.3847/1538-4357/ad7a6f)

Saeedzadeh, V., Mukherjee, S., Babul, A., Tremmel, M., & Quinn, T. R. 2024b, MNRAS, 529, 4295, doi: [10.1093/mnras/stae513](https://doi.org/10.1093/mnras/stae513)

Saeedzadeh, V., Jung, S. L., Rennehan, D., et al. 2023, MNRAS, 525, 5677, doi: [10.1093/mnras/stad2637](https://doi.org/10.1093/mnras/stad2637)

Schaye, J., Crain, R. A., Bower, R. G., et al. 2015, MNRAS, 446, 521, doi: [10.1093/mnras/stu2058](https://doi.org/10.1093/mnras/stu2058)

Schaye, J., Chaikin, E., Schaller, M., et al. 2025, arXiv, doi: [10.48550/arXiv.2508.21126](https://doi.org/10.48550/arXiv.2508.21126)

Schiminovich, D., Wyder, T. K., Martin, D. C., et al. 2007, ApJS, 173, 315, doi: [10.1086/524659](https://doi.org/10.1086/524659)

Shen, S., Yang, X., Mo, H., van den Bosch, F., & More, S. 2014, ApJ, 782, 23, doi: [10.1088/0004-637X/782/1/23](https://doi.org/10.1088/0004-637X/782/1/23)

Smith, B. D., Bryan, G. L., Glover, S. C. O., et al. 2017, MNRAS, 466, 2217, doi: [10.1093/mnras/stw3291](https://doi.org/10.1093/mnras/stw3291)

Somerville, R. S., & Davé, R. 2015, ARA&A, 53, 51, doi: [10.1146/annurev-astro-082812-140951](https://doi.org/10.1146/annurev-astro-082812-140951)

Stinson, G., Seth, A., Katz, N., et al. 2006, MNRAS, 373, 1074, doi: [10.1111/j.1365-2966.2006.11097.x](https://doi.org/10.1111/j.1365-2966.2006.11097.x)

Storn, R., & Price, K. 1997, JOGO, 11, 341, doi: [10.1023/A:1008202821328](https://doi.org/10.1023/A:1008202821328)

Su, K.-Y., Hopkins, P. F., Bryan, G. L., et al. 2021, MNRAS, 507, 175, doi: [10.1093/mnras/stab2021](https://doi.org/10.1093/mnras/stab2021)

Tacchella, S., Conroy, C., Faber, S. M., et al. 2022, ApJ, 926, 134, doi: [10.3847/1538-4357/ac449b](https://doi.org/10.3847/1538-4357/ac449b)

Talbot, Jr., R. J., & Arnett, W. D. 1971, ApJ, 170, 409, doi: [10.1086/151228](https://doi.org/10.1086/151228)

Talbot, R. Y., Bourne, M. A., & Sijacki, D. 2021, MNRAS, 504, 3619, doi: [10.1093/mnras/stab804](https://doi.org/10.1093/mnras/stab804)

Taranu, D. S., Hudson, M. J., Balogh, M. L., et al. 2014, MNRAS, 440, 1934, doi: [10.1093/mnras/stu389](https://doi.org/10.1093/mnras/stu389)

Toni, G., Maturi, M., Finoguenov, A., Moscardini, L., & Castignani, G. 2024, A&A, 687, A56, doi: [10.1051/0004-6361/202348832](https://doi.org/10.1051/0004-6361/202348832)

Tremmel, M., Governato, F., Volonteri, M., & Quinn, T. R. 2015, MNRAS, 451, 1868, doi: [10.1093/mnras/stv1060](https://doi.org/10.1093/mnras/stv1060)

Tremmel, M., Karcher, M., Governato, F., et al. 2017, MNRAS, 470, 1121, doi: [10.1093/mnras/stx1160](https://doi.org/10.1093/mnras/stx1160)

Tremmel, M., Wright, A. C., Brooks, A. M., et al. 2020, MNRAS, 497, 2786, doi: [10.1093/mnras/staa2015](https://doi.org/10.1093/mnras/staa2015)

Tremmel, M., Quinn, T. R., Ricarte, A., et al. 2019, MNRAS, 483, 3336, doi: [10.1093/mnras/sty3336](https://doi.org/10.1093/mnras/sty3336)

van de Voort, F., Springel, V., Mandelker, N., van den Bosch, F. C., & Pakmor, R. 2019, MNRAS: Letters, 482, L85, doi: [10.1093/mnrasl/sly190](https://doi.org/10.1093/mnrasl/sly190)

Van Kempen, W., Cluver, M., Jarrett, T., et al. 2024, PASA, 41, e096, doi: [10.1017/pasa.2024.97](https://doi.org/10.1017/pasa.2024.97)

Vogelsberger, M., Marinacci, F., Torrey, P., & Puchwein, E. 2020, Nat Rev Phys, 2, 2, doi: [10.48550/arXiv.1909.07976](https://doi.org/10.48550/arXiv.1909.07976)

Von Der Linden, A., Best, P. N., Kauffmann, G., & White, S. D. M. 2007, MNRAS, 379, 867, doi: [10.1111/j.1365-2966.2007.11940.x](https://doi.org/10.1111/j.1365-2966.2007.11940.x)

Weaver, J. R., Kauffmann, O. B., Ilbert, O., et al. 2022, ApJS, 258, 11, doi: [10.3847/1538-4365/ac3078](https://doi.org/10.3847/1538-4365/ac3078)

Weinberger, R., Springel, V., Hernquist, L., et al. 2017, MNRAS, 465, 3291, doi: [10.1093/mnras/stw2944](https://doi.org/10.1093/mnras/stw2944)

Weinmann, S. M., van den Bosch, F. C., Yang, X., & Mo, H. J. 2006, MNRAS, 366, 2, doi: [10.1111/j.1365-2966.2005.09865.x](https://doi.org/10.1111/j.1365-2966.2005.09865.x)

Whitaker, K. E., van Dokkum, P. G., Brammer, G., & Franx, M. 2012, ApJL, 754, L29, doi: [10.1088/2041-8205/754/2/L29](https://doi.org/10.1088/2041-8205/754/2/L29)

Wuyts, S., Förster Schreiber, N. M., Lutz, D., et al. 2011, ApJ, 738, 106, doi: [10.1088/0004-637X/738/1/106](https://doi.org/10.1088/0004-637X/738/1/106)

Yoon, Y., Im, M., & Kim, J.-W. 2017, ApJ, 834, 73, doi: [10.3847/1538-4357/834/1/73](https://doi.org/10.3847/1538-4357/834/1/73)

Zhao, D., Aragón-Salamanca, A., & Conselice, C. J. 2015a, MNRAS, 448, 2530, doi: [10.1093/mnras/stv190](https://doi.org/10.1093/mnras/stv190)

Zhao, D., Aragón-Salamanca, A., & Conselice, C. J. 2015b, MNRAS, 453, 4444, doi: [10.1093/mnras/stv1940](https://doi.org/10.1093/mnras/stv1940)